Available online at www.sciencedirect.com
SCIENCE DIRECT®
Journal of Computational Physics 215 (2006) 98–132
JOURNAL OF COMPUTATIONAL PHYSICS
www.elsevier.com/locate/jcp

Hydrodynamic simulation of air bubble implosion using a level set approach

Sunitha Nagrath [a,c,1], Kenneth Jansen [a,c,*], Richard T. Lahey Jr. [b,c], Iskander Akhatov [d]

[a] Scientific Computation Research Center, CII-7013, Rensselaer Polytechnic Institute, Troy, NY 12180, USA
[b] Center for Multiphase Research, Rensselaer Polytechnic Institute, Troy, NY 12180, USA
[c] Department of Mechanical, Aerospace and Nuclear Engineering, Rensselaer Polytechnic Institute, Troy, NY 12180, USA
[d] Department of Mechanical Engineering and Applied Mechanics, North Dakota State University, Fargo, ND, USA

Received 8 April 2005; received in revised form 25 October 2005; accepted 26 October 2005
Available online 27 December 2005

Abstract

The hydrodynamics of the implosion and rebound of a small (10 μm diameter) air bubble in water was studied using a three-dimensional direct numerical simulation (DNS). To study this problem, we developed a novel stabilized finite element method (FEM) employing a combination of ghost fluid and level set approaches. This formulation treats both the air and water as compressible fluids. Using this method, a transient three-dimensional (3-D) solution was obtained for the implosion (i.e., collapse) and rebound of an air bubble. These simulation results obtained were qualitatively similar to those observed/predicted in previous experimental/numerical studies. The 3-D simulations show that the conditions within the bubble are nearly uniform until the converging pressure wave is strong enough to create very large temperatures and pressures near the center of the bubble. These dynamics occur on very small spatial (0.1–0.7 μm), and time (ns) scales. The motion of the air/water interface during the initial stages of the implosion was found to be consistent with predictions using a Rayleigh–Plesset model. However, the simulations showed that during the final stage of energetic implosions, the bubble can become asymmetric, which is contrary to the spherical symmetry assumed in many previous numerical studies of bubble dynamics. The direct numerical simulations predicted two different instabilities, namely Rayleigh–Taylor type interfacial/surface and shape instabilities. During the violent collapse stage, the bubble deviates from spherical symmetry and deforms into an ellipsoidal-shaped bubble. A linear stability analysis based on spherical harmonics also indicates that an ellipsoidal bubble shape could be expected. Moreover, interfacial instabilities also appear during the later stage of the implosion process. Distinguishing these phenomena with the help of numerical simulations opens new opportunities to understand many features of recent experiments on sonoluminescence and sonofusion.

Keywords: Finite element; Level set; Bubble implosion; Two phase-flow

* Corresponding author. Tel.: +1 617 724 6819; fax: +1 617 724 2999.
E-mail addresses: sunitha_nagrath@hms.harvard.edu (S. Nagrath), kjansen@scorec.rpi.edu (K. Jansen), laheyr@rpi.edu (R.T. Lahey Jr.), Iskander.Akhatov@ndsu.nodak.edu (I. Akhatov).
[1] Present address: Harvard Medical School/MGH, Surgery, Bldg #114, 16th Street, Charlestown, MA 02129, USA.

0021-9991/$ - see front matter
doi:10.1016/j.jcp.2005.10.020

1. Introduction

The violent implosion of vapor/gas bubbles may lead to a number of phenomena of interest in science and engineering including; cavitation damage, sonoluminescence, sonochemistry, sonofusion, etc. Owing to their great practical importance, scientists and engineers have made a substantial effort to understand the hydrodynamics involved through both experimental and theoretical investigations. Pioneering work on cavitation and bubble dynamics was done by Rayleigh [44], who considered both empty and the gas filled cavities collapsing in an incompressible liquid, but neglected surface tension and viscous effects. The Rayleigh–Plesset equation [44,28,42,35] extended Rayleigh's analysis to include surface tension and viscosity. Subsequently, many researchers have refined these analyses by considering the effect of thermal conduction in the gas [39,38], and accounting for the compressibility of the surrounding liquid [17,43,30,37]. However, none of these studies treated the gas phase in detail since they assumed hydrodynamic equilibrium in the gas phase.

Indeed, many of these models also assumed that the gas was homobaric and was heated isentropically. During bubble implosions experimental findings indicate gas temperatures on the order of at least several thousand degrees Kelvin, which implies a very high compression of the gas phase. To better understand the gas compression process, researchers [63,33,37] have considered more complete solutions to the equations of motion. The numerical studies of Wu and Roberts [63] showed that a shock can occur inside the gas bubble. However this study was performed assuming spherical symmetry (i.e., considering only spatial variations in the radial direction). The most detailed numerical studies published to date were those of Moss et al. [33] and Yu et al. [66]. Unlike Wu and Roberts [63], these authors did not obtain the dynamics of the bubble from the Rayleigh–Plesset equation. Rather they performed a complete analysis of the non-linear hydrodynamics of the liquid surrounding the bubble using finite difference discretization of the conservation laws. However, the analysis by Moss et al. [33] was unsteady but one-dimensional. Furthermore, they did not consider viscous and surface tension effects. On the other hand, Yu et al. [66] solved the Navier–Stokes equations in 3-D using a finite difference/front tracking technique, but they assumed that the surrounding fluid was incompressible, and the pressure inside the bubble was uniform and neglected thermal effects.

The previous studies recognized the fact that an analysis based on spherical symmetry cannot be rigorously correct [42], and hence researchers have attempted to study the spherical shape oscillations theoretically. Hilgenfeldt et al. [18] elucidated for the first time the phase diagram for stable single bubble sonoluminescence (SL) considering both shape and diffusion instabilities. Yuan et al. [67] numerically studied the shape stability of a radially oscillating gas bubble by using the theoretical model of Hilgenfeldt et al. [18] with corrections taking into account the gas density effect. Nevertheless, the authors suggest that further study, free from the spherical symmetry assumption, would be necessary to understand the complete dynamics of bubble shape instabilities. Previous researchers [5,18] also noted the significance of identifying these instabilities, and they suggested that the Rayleigh–Taylor (RT) shape instabilities were likely responsible for the extinction of SL when the acoustic field driving the bubble oscillation exceeds a certain threshold; in particular, about 1.7 bar for an air/water system [1].

However, very few attempts [66] have been made to solve the full three-dimensional (3-D) non-linear problem to study the temporal evolution of these instabilities. The analysis of the collapse and rebound of an imploding bubble is complex due to the highly transient and non-linear nature of the problem. In this paper, we have presented a detailed 3-D analysis considering effects of viscosity and surface tension and the complete set of the conservation laws (i.e., the conservation of mass, momentum, and energy) for both the compressible liquid and gas phases. The dynamics of the bubble is implicitly obtained as a part of the solution rather than from a Rayleigh–Plesset analysis. The following discussion provides the motivation for the direct numerical simulation (DNS) of bubble dynamics.

In an effort to learn more about the dynamics of the bubble and shock wave interaction, researchers traditionally carry out experiments. However, the phenomena of interest here occurs on very small spatial and time scales, which makes instrumentation and accurate measurements difficult. Hence, despite the advances in technology, experimentalists continue to have difficulties in studying the dynamics of bubble implosion processes. While the overall characteristics of the bubble dynamics is of interest, the implosion process, which is strongly influenced by the evolution of the smallest scales, is the key to understanding phenomena such as cavitation damage, sonoluminescence and sonofusion. The search for new alternatives to understand the

hydrodynamics involved has resulted in the development of various numerical techniques. However, the development of efficient algorithms to understand rapid bubble dynamics is still a challenge.

Owing to the advances in numerical methods and computational hardware, numerical experiments have become increasingly popular and feasible for the study of complex non-linear systems. Direct numerical simulations (DNS) offer an excellent opportunity to understand bubble dynamics and allows new insights into key mechanisms during bubble implosions. Nevertheless, the development of a method to study complex problems such as an air bubble implosion, presents a number of challenges. The foremost challenge is to efficiently represent the coupled compressible fluid dynamics of both phases (liquid and gas). Secondly, the method must allow one to accurately track the interface between the phases. Finally, it must be capable of resolving any shock waves which may be created in one or both phases during the final stage of bubble implosion.

In all multiphase numerical methods, the essential ingredients are an efficient technique to evaluate the phasic flow fields, and an accurate and robust strategy to resolve the interface. A detailed discussion of the various available multiphase methods has been presented by Nagrath et al. [34]. Although over the last several decades, finite element methods have grown in popularity for fluid dynamics applications, not until recently has this method been used to study multiphase flow problems [34,57,56,2,53,54]. Tezduyar et al. [53] developed a front tracking method to resolve interfaces using deforming space-time finite element formulations. Barth and Sethian [2] developed a finite element Petrov–Galerkin scheme for the level set equations on triangulated domains. Tornberg and Engquist [57] presented a numerical method for simulating incompressible two-dimensional multiphase flow. Nagrath et al. [34] presents a finite element level set method for solving incompressible multiphase flows in three dimensions. This paper extends the aforementioned works to present for the first time a three-dimensional stabilized finite element level set approach for solving two-phase compressible flows. In the present work, a stabilized finite element method (FEM) namely, a streamline upwind Petrov–Galerkin (SUPG) method, was employed for computing both the flow fields and the interface motion. The finite element method (FEM) has the advantage of using an unstructured mesh to match the grid size to the required local physical length scales [32]. Additionally, the method has been proven to be stable and to attain optimal convergence rates with respect to the interpolation errors [13,20]. As discussed by Hughes et al. [21], the SUPG method is an excellent method for problems with smooth solutions, but typically introduces localized oscillations about sharp internal features and boundary layers. To prevent oscillations, a discontinuity-capturing term, proposed by Hughes et al. [22], was added to the formulation. This term provides additional control over gradients in the discrete solution and considerably increases the robustness of the methodology. In the current work, we have used the level set method for computing interface motion. The strength of this method lies in its ability to efficiently represent an arbitrarily complex interface accurately, thereby allowing the computation of flows with surface tension and rapidly changing topology.

The continuum surface force (CSF) model proposed by Brackbill et al. [4] was implemented to incorporate surface-tension-induced stresses. Also, an efficient re-distancing strategy [40] was adopted to ensure the volume of each phase was conserved during re-distancing. Although the proposed algorithm is known to predict compressible gas dynamics quite well for compressible multiphase flows, it can lead to the spurious non-physical oscillations across the interface due to smeared density profiles. This can be attributed to the radical change in the equations of state across the interface. Hence, an approach similar to the ghost fluid method developed by Fedkiw et al. [11] in the finite difference context, has been developed and implemented into our finite element model. This model allowed us to treat compressible multiphase flows with large density differences. It should be stressed that the strategy and FEM formulations presented in this paper, employing both ghost fluid and level set methods, are novel in the field of computational fluid dynamics and are well suited for the analysis of compressible 3-D multiphase flows.

With numerical simulations, we show that due to the inertial effect of the liquid compressing the gas, an energetic bubble implosion may take place. During bubble collapse, the simulations predict spherically converging shock wave development, which intensifies as it moves towards the center of the bubble. This shock causes the local temperatures and pressures of the air in the interior of the bubble to rise rapidly. The air bubble reaches a minimum radius at the end of the implosion and then rebounds due to high internal gas pressure. The reflection of the shock from the center of the bubble produces a spherically divergent shock wave. Additionally, it was observed that, during the final stages of collapse, the bubble experiences two different instabilities: (i) interfacial instabilities, which occur whenever the gas is strongly accelerated into

a liquid; (ii) shape instabilities due to the excitation of non-spherical modes causing the bubble to take on a non-spherical shape. These instabilities are in good agreement with earlier numerical and theoretical predictions. As noted by Wu and Roberts [64], the classical RT surface instabilities that arise on the surface of an acoustically-driven bubble are complicated by the spherical geometry, by the temporally varying accelerations, and by the possibility of resonances between the oscillations in bubble shape and the driving frequency. The Rayleigh–Taylor (RT) interfacial instabilities, which arise due to the significant difference in the momentum across the interface, quickly vanish once the phasic density difference vanishes and when the rebounding bubble expands.

The outline of the paper is as follow: Section 2 presents a theoretical prediction of the motion of the bubble and the pressure and velocity fields inside the gas and liquid phase during the initial stages of a bubble implosion. Section 3 presents the formulations and the numerical method, which includes the governing conservation equations (Section 3.1), the level set method (Section 3.2) and surface tension modeling (Section 3.3). The finite element discretization of the compressible Navier–Stokes equations is presented in Section 4. The discontinuity capturing operator, implemented to efficiently perform the flow computations with sharp discontinuities or shocks, is discussed in Section 4.1. Also in this section, we present the modeling details of the level set method and the finite element solution technique for solving both the level set and the re-distancing equations (Section 4.2). The novel approach used to implement the ghost fluid method is discussed in Section 4.3. Section 5 presents the results and discussion and Section 6 presents the salient conclusions.

2. Bubble motion and flow field during the initial stages of implosion

The collapse of a spherical gas filled cavity in an incompressible fluid can be determined using the Rayleigh equation [44]. Knowing the evolution of bubble radius, one can calculate the evolution of the pressure and flow field. This process is well described by Nigmatulin et al. [37]. The following analysis describes how to obtain the flow field based during the low Mach number phase of bubble implosion. DNS does not necessarily require this solution, however, this analysis can be used to generate the appropriate initial conditions for the early stages of bubble implosion and this will save computational resources. The details of its use are given in Section 5.3.

Consider the spherically symmetric radial flow of an incompressible liquid inside an infinitely large spherical domain. A gas bubble is located at the center of the domain. The momentum balance of the surrounding liquid in radial direction is given by

$$\rho_l\left(\frac{\partial u}{\partial t}+u\frac{\partial u}{\partial r}\right)=-\frac{\partial p}{\partial r}, \tag{1}$$

where r is the radial distance from center of the bubble, and u is the velocity in the radial direction. If $R(t)$ is the instantaneous bubble radius, then the conservation of mass for an incompressible liquid dictates that

$$u=\frac{R^2\dot{R}}{r^2}. \tag{2}$$

Since the radial velocity can be expressed in terms of a velocity potential as, $u=\frac{\partial \Phi}{\partial r}$, we can write,

$$\Phi=\frac{-R^2\dot{R}}{r}. \tag{3}$$

Substituting (3) in (1) yields

$$\rho_l\left[\frac{\partial}{\partial r}\left(\frac{\partial \Phi}{\partial t}\right)+\frac{\partial}{\partial r}\left(\frac{u^2}{2}\right)\right]+\frac{\partial p}{\partial r}=0. \tag{4}$$

Integrating the above equation with respect to "r" yields the transient Bernoulli equation,

$$\rho_l\left[\frac{\partial \Phi}{\partial t}+\frac{u^2}{2}\right]+p=F(t). \tag{5}$$

As $r \to \infty$, $\Phi = 0$, $p = p_\infty$, so, $F(t) = p_\infty$. Therefore,

$$p = p_\infty - \rho_1\left(\frac{\partial \Phi}{\partial t} + \frac{u^2}{2}\right). \tag{6}$$

Substituting for Φ and u in terms of "R", using (2) and (3), we have,

$$p(r,t) = p_\infty - \rho_1\left[-\frac{R^2\ddot{R}}{r} - \frac{2R\dot{R}^2}{r} + \frac{\dot{R}^2R^4}{2r^4}\right]. \tag{7}$$

Applying (7) at point $r = R(t)$, we obtain the well-known Rayleigh equation,

$$R\ddot{R} + \frac{3}{2}\dot{R}^2 = \frac{(p_a - p_\infty)}{\rho_1}, \tag{8}$$

where p_a is the liquid pressure at the liquid/bubble interface (uniform pressure within the bubble is assumed for the initial conditions, and this is a valid assumption for the initial phase of bubble collapse) given by

$$p_a = \left(p_0 + \frac{2\sigma}{R_0}\right)\left(\frac{R_0}{R}\right)^{3\gamma} - \frac{2\sigma}{R}. \tag{9}$$

Here R_0 is the initial bubble radius at $t = 0$, p_0 is the liquid equilibrium pressure when the gas bubble is at its initial radius, and γ is the polytropic exponent of the gas. For isothermal conditions $\gamma = 1$, where for adiabatic conditions γ is the ratio of the specific heats $(\frac{C_p}{C_v})$. Combining (8) and (7) yields an equation governing the pressure distribution in the liquid,

$$p(r,t) = p_\infty\left[1 - \frac{R}{r}\right] + p_a\frac{R}{r} + \rho_1\frac{R\dot{R}^2}{2r}\left[1 - \frac{R^3}{r^3}\right]. \tag{10}$$

The FEM based hydrodynamic shock code, which is primarily focus of this paper can be initialized using (7) and (2).

3. Numerical formulation

3.1. Governing equations

Consider the compressible equations of motion (complete with the continuity and total energy equations) written in conservative form [24,25]

$$\boldsymbol{U}_{,t} + \boldsymbol{F}^{\text{adv}}_{i,i} - \boldsymbol{F}^{\text{diff}}_{i,i} = \mathscr{S}, \tag{11}$$

where

$$\boldsymbol{U} = \{\, U_1 \quad U_2 \quad U_3 \quad U_4 \quad U_5 \,\}^{\mathrm{T}} = \rho\{\, 1 \quad u_1 \quad u_2 \quad u_3 \quad e_{\text{tot}} \,\}^{\mathrm{T}}, \tag{12}$$

$$\boldsymbol{F}^{\text{adv}}_i = u_i\boldsymbol{U} + p\{\, 0 \quad \delta_{1i} \quad \delta_{2i} \quad \delta_{3i} \quad u_i \,\}^{\mathrm{T}}, \tag{13}$$

$$\boldsymbol{F}^{\text{diff}}_i = \{\, 0 \quad \tau_{1i} \quad \tau_{2i} \quad \tau_{3i} \quad \tau_{ij} \quad u_j - q''_i \,\}^{\mathrm{T}} \tag{14}$$

and

$$\tau_{ij} = 2\mu\left(S_{ij}(\boldsymbol{u}) - \frac{1}{3}S_{kk}(\boldsymbol{u})\delta_{ij}\right), \quad S_{ij}(\boldsymbol{u}) = \frac{u_{i,j} + u_{j,i}}{2}, \tag{15}$$

$$q''_i = -\kappa T_{,i}, \quad e_{\text{tot}} = e + \frac{u_iu_i}{2}, \quad e = c_vT. \tag{16}$$

The state variables are: the velocity u_i, the pressure p, the density ρ, the temperature T and the total convected specific energy e_{tot}. Constitutive laws relate the stress, τ_{ij}, to the deviatoric portion of the strain, $S^{\text{d}}_{ij} = S_{ij} - \frac{1}{3}S_{kk}\delta_{ij}$, through a molecular viscosity, μ. Similarly, the heat flux, q''_i, is proportional to the gradient of temperature with the proportionality constant being the molecular thermal conductivity, κ. The

formulations presented in this work can accommodate a general divariant fluid. A variety of equations of state can be considered, however in this study, the gas phase was assumed to be an ideal gas and the liquid phase was described by a linearly compressible equation of state. Note that we have two fluids (with two viscosities, two thermal conductivities and two constitutive laws), however, as will be discussed later, a level set field, ϕ, allows us to consider these fields as one global field for each varying quantity. Finally, $\mathscr{S}$ is a body force (or source) term, such as gravity, and the force due to the surface tension. The representation of the interfacial surface tension force as a "body force" applied on the interface is dealt with in Section 3.3.

For the specification of the methods that follow, it is helpful to define a quasi-linear operator (with respect to some, yet to be determined, state variable vector, $\boldsymbol{Y}$, defined in (37)) related to (11) as

$$\mathscr{L} \equiv \boldsymbol{A}_0 \frac{\partial}{\partial t} + \boldsymbol{A}_i \frac{\partial}{\partial x_i} - \frac{\partial}{\partial x_i}\left(\boldsymbol{K}_{ij} \frac{\partial}{\partial x_j}\right), \tag{17}$$

which can be decomposed into time, advective, and diffusive portions,

$$\mathscr{L} = \mathscr{L}_t + \mathscr{L}_{\text{adv}} + \mathscr{L}_{\text{diff}}. \tag{18}$$

Here $\boldsymbol{A}_i = \boldsymbol{F}^{\text{adv}}_{i,\boldsymbol{Y}}$ is the ith Euler–Jacobian matrix, $\boldsymbol{K}_{ij}$ is the diffusivity matrix, defined such that $\boldsymbol{K}_{ij}\boldsymbol{Y}_{,j} = \boldsymbol{F}^{\text{diff}}_i$, and $\boldsymbol{A}_0 = \boldsymbol{U}_{,\boldsymbol{Y}}$ is the change of variables metric, which can be found in Appendix A. For a complete description of matrices $\boldsymbol{A}_0$, $\boldsymbol{A}_i$ and $\boldsymbol{K}_{ij}$, the reader is referred to Hauke [14]; Hauke and Hughes [16]. Using these results, one can write (11) as simply, $\mathscr{L}\boldsymbol{Y} = \mathscr{S}$.

3.2. The level set method

The level set approach represents the interface as a zero level set of a smooth function, and simultaneously maintains a level set function, which, by definition, is the signed distance from the interface. Hence, instead of explicitly tracking the interface, we implicitly "capture" the interface within a field which is interpolated with the finite element basis functions like any other state variable (e.g. pressure, velocity, temperature, etc.). This enables us to represent the interface between the two phases accurately and to compute flows with large density ratios and surface tension. As noted by Sussman et al. [51], conventional conservative methods suffer from excessive numerical diffusion which smears the sharpness of the front. The level set function is typically a smooth (Lipschitz continuous) function, denoted here as ϕ, which eliminates the difficulties that conventional conservative schemes incur.

Probably, the most important advantage of level set methods is that the interfaces can easily merge or break-up. Furthermore, the level set formulation generalizes easily to three dimensions. The actual location of the interface is never computed, since the interface is embedded as a particular level set in a fixed domain.

In our formulations, a smooth level set function, ϕ, was used to track the interface between the gas phase and the liquid phase. The interface, Γ', is the zero level set of ϕ

$$\Gamma' = \{\boldsymbol{x} | \phi(\boldsymbol{x}, t) = 0\}. \tag{19}$$

The level set function is considered here to be positive in the liquid phase and negative in the gas phase. Hence we have:

$$\phi(\boldsymbol{x}, t) = \begin{cases} > 0 & \text{if } \boldsymbol{x} \in \text{the liquid}, \\ 0 & \text{if } \boldsymbol{x} \in \Gamma', \\ < 0 & \text{if } \boldsymbol{x} \in \text{the gas}. \end{cases} \tag{20}$$

Therefore, we initialize ϕ to be the signed normal distance from the interface. Since the interface moves with the fluid, the evolution of ϕ is governed by a transport equation

$$\frac{\boldsymbol{D}\phi}{\boldsymbol{D}t} = \frac{\partial \phi}{\partial t} + \boldsymbol{u} \cdot \nabla \phi = 0. \tag{21}$$

As discussed in Section 4.2, this additional advection equation for the level set scalar is solved in a manner similar to the equations of motion. The physical properties of the fluid in each phase are calculated as a function of ϕ as:

$$\rho(\phi) = \rho_1 H(\phi) + \rho_2(1 - H(\phi)), \tag{22}$$

$$\mu(\phi) = \mu_1 H(\phi) + \mu_2(1 - H(\phi)), \tag{23}$$

where $H(\phi)$ is the Heaviside function given by:

$$H(\phi) = \begin{cases} 0 & \text{if } \phi < 0, \\ \frac{1}{2} & \text{if } \phi = 0, \\ 1 & \text{if } \phi > 0. \end{cases} \tag{24}$$

3.2.1. Interface thickness

Use of the Heaviside function described above leads to poor numerical results due to the assumed zero thickness of the interface. Instead, we can use an alternative description of the interface as proposed by Sussman et al. [51]; Unverdi and Tryggvason [58]; and Sussman et al. [48]. It should be noted that there exist another approach proposed by Kang et al. [27] which treats the interface in a sharp fashion using jump conditions at the interface. However, in the present work, we took the former approach and used a smoothed Heaviside function, $H_\epsilon(\phi)$, instead of the exact Heaviside function, $H(\phi)$. The smooth Heaviside function was defined as [48]:

$$H_\epsilon(\phi) = \begin{cases} 0 & \text{if } \phi < -\epsilon, \\ \frac{1}{2}\left[1 + \frac{\phi}{\epsilon} + \frac{1}{\pi}\sin\left(\frac{\pi\phi}{\epsilon}\right)\right] & \text{if } |\phi| \leqslant \epsilon, \\ 1 & \text{if } \phi > \epsilon, \end{cases} \tag{25}$$

where ϕ represents the signed normal distance to the interface. The $\frac{1}{2}$ contour of the sharp Heaviside function $H(\phi)$ creates jagged or staircase contours on any discrete mesh of spacing Δx. However, by giving the interface a thickness of $\epsilon = \lambda\Delta x$, where $\lambda > 1$, sharp changes across the interface are smoothed.

3.2.2. Re-initialization or re-distancing of level sets

In the formulation describe above, the interface will be accurate so long as ϕ is maintained as a distance function. However, under the convection implied by Eq. (21), the level sets that are adjacent to the zero level set may move with velocities different than that of the zero level set. If so, the ϕ distance field will get distorted. Thus, one must re-distance the level set function on regular intervals in order to rebuild/maintain the signed distance function. There are several ways to accomplish this re-distancing [10,49–51]. We have followed the technique introduced by Sussman et al. [51]. Its virtue is that the level set function can be re-initialized without explicitly finding the zero level set. The idea is to solve the partial differential equation,

$$\frac{\partial d}{\partial \tau^d} = S(\phi)(1 - |\nabla d|), \tag{26}$$

where

$$S(\phi) = \begin{cases} -1 & \text{if } \phi < 0, \\ 0 & \text{if } \phi = 0, \\ 1 & \text{if } \phi > 0 \end{cases} \tag{27}$$

and $d(\boldsymbol{x},\tau^d = 0) = \phi(\boldsymbol{x},t)$ and τ^d is a pseudo time. Given any initial data for ϕ, solving this equation to steady-state provides the distance field ϕ with the required property $|\nabla\phi| = 1$, since convergence occurs when the right hand side of (26) is zero. Note that the sign function $S(\phi)$ controls the flow of information. If ϕ is negative, information flows from the interface into the gas (i.e., more negative ϕ), and if ϕ is positive, information flows the opposite way. The net effect is to re-distance the level sets on either side of the zero level set. Furthermore, instead of the sharp sign function we use the smooth sign function defined as

$$S(\phi) = 2(H_\epsilon(\phi) - 1/2), \tag{28}$$

where $H_\epsilon(\phi)$ is given by (25). The steady solutions of (26), d, are distance functions. Since, on the interface $S(0) = 0$, $d(\boldsymbol{x},\tau^d)$ has the same zero level set as $\phi(\boldsymbol{x},t)$. Note, that this equation is relaxed in pseudo-time, τ^d,

which is not related to the physical time, t. Hence we only need to solve (26) for $\tau^d = 0 \ldots \epsilon \boldsymbol{v}$, because the level set function re-initialization is required only near the interface. The definition of $\boldsymbol{v}$ is obvious if we re-write (26) in hyperbolic form as [51]

$$\frac{\partial d}{\partial \tau^d} + \boldsymbol{v} \cdot \nabla d = S(\phi), \tag{29}$$

where the pseudo-convection speed is given by

$$\boldsymbol{v} = S(\phi)\frac{\nabla d}{|\nabla d|}. \tag{30}$$

Eq. (29) is a non-linear hyperbolic equation with characteristics pointing outwards from the interface in the direction of the normal. The numerical strategy, which was adopted in the present study, was to perform the re-distancing operation at the end of each time step.

3.3. Modeling of surface tension

For many fluid flow problems interfacial motion induced by surface tension may play a significant role. Surface tension creates a microscopic, localized surface force that exerts itself in both the tangential and normal directions. We have used the continuum approach proposed by Brackbill et al. [4] in order to represent the surface tension force as a body force. This model represents surface tension as a continuous three-dimensional effect across an interface, rather than as a boundary value at the interface. The resulting "body force" due to surface tension can be written as

$$f = -\frac{\kappa(\phi)\nabla H_\epsilon(\phi)}{We}, \tag{31}$$

where $\kappa(\phi)$ is the interfacial curvature given by

$$\kappa(\phi) = \nabla \cdot \left(\frac{\nabla \phi}{|\nabla \phi|}\right), \tag{32}$$

$H_\epsilon(\phi)$ is the Heaviside function as defined in (25), and We is the Weber number, which is given by

$$We = \frac{\rho_1 L U^2}{\sigma}, \tag{33}$$

where L and U are the reference length and the velocity. The surface tension term and local interfacial curvature are easily represented in terms of the level set function. Indeed, since the level set function in our formulations is just the signed distance from the interface, the curvature can be accurately computed from the level set function. However, the calculation of curvature involves second order derivatives, and since we used piecewise-linear basis functions, these second derivatives are zero on the element interior. Hence, the piecewise-constant gradients were reconstructed to be continuous, using an L_2 projection, and then the second order derivatives were evaluated by differentiating the reconstructed gradient. This procedure is described in detail by Jansen et al. [26]. The form of the surface tension force as a "body force" used herein is due to Chang et al. [8].

4. Discretization

To proceed with the finite element discretization of the equations of motion, (11), we must define the finite element approximation spaces. Let $\overline{\Omega} \subset \mathbf{R}^N$ represent the closure of the physical spatial domain (i.e., $\Omega \cup \Gamma$ where Γ is the boundary) in N dimensions; where $N = 3$ is considered here. The boundary is decomposed into portions with natural boundary conditions, Γ_h, and essential boundary conditions, Γ_g, i.e., $\Gamma = \Gamma_g \cup \Gamma_h$. In addition, $H^1(\Omega)$ represents the usual Sobolev space of functions with square-integrable values and derivatives on Ω.

Next, Ω is discretized into n_{el} finite elements, Ω^e. With this, we may define the trial solution space for the semi-discrete formulations as

$$\mathscr{V}_h = \{\boldsymbol{v}|\boldsymbol{v}(\cdot,t) \in H^1(\Omega)^m,\ t \in [0,T],\ \boldsymbol{v}|_{x\in\Omega^e} \in P_k(\Omega^e)^m,\quad \boldsymbol{v}(\cdot,t) = \boldsymbol{g} \text{ on } \Gamma_g\} \tag{34}$$

and the weight function space as

$$\mathscr{W}_h = \{\boldsymbol{w}|\boldsymbol{w}(\cdot,t) \in H^1(\Omega)^m,\ t \in [0,T],\ \boldsymbol{w}|_{x\in\Omega^e} \in P_k(\Omega^e)^m,\quad \boldsymbol{w}(\cdot,t) = 0 \text{ on } \Gamma_g\}, \tag{35}$$

where $P_k(\Omega^e)$, is the space of all polynomials defined on Ω^e, complete to order $k \geqslant 1$, and m is the number of degrees of freedom ($m = 5$).

To derive the weak form of (11), the entire equation is dotted with a vector of weight functions, $\boldsymbol{W} \in \mathscr{W}_h$, and integrated over the spatial domain. Integration by parts is then performed to move the spatial derivatives onto the weight functions thus decreasing the continuity requirements. This process leads to an integral equation (often referred to as the weak form), where find $\boldsymbol{Y} \in \mathscr{V}_h$ such that

$$\begin{aligned} 0 = &\int_\Omega (\boldsymbol{W}\cdot\boldsymbol{A}_0\boldsymbol{Y}_{,t} - \boldsymbol{W}_{,i}\cdot\boldsymbol{F}_i^{\text{adv}} + \boldsymbol{W}_{,i}\cdot\boldsymbol{F}_i^{\text{diff}} + \boldsymbol{W}\cdot\mathscr{S})\,\mathrm{d}\Omega - \int_\Gamma \boldsymbol{W}\cdot\left(-\boldsymbol{F}_i^{\text{adv}} + \boldsymbol{F}_i^{\text{diff}}\right)n_i\,\mathrm{d}\Gamma \\ &+ \sum_{e=1}^{n_{\text{el}}}\int_{\Omega^e} \mathscr{L}^{\mathrm{T}}\boldsymbol{W}\cdot\boldsymbol{\tau}(\mathscr{L}\boldsymbol{Y} - \mathscr{S})\,\mathrm{d}\Omega. \end{aligned} \tag{36}$$

The first and second lines of (36) contains the Galerkin approximation (interior and boundary, respectively) and the last line contains the least-squares stabilization. Note that the stream line upwind Petrov–Galerkin (SUPG) [7] stabilization is obtained by replacing $\mathscr{L}^{\mathrm{T}}$ by $\mathscr{L}^{\mathrm{T}}_{\text{adv}}$. The stabilization matrix $\boldsymbol{\tau}$ is an important ingredient in these methods and it has been well documented by Shakib [46]; Franca and Frey [13]. Note that we have chosen to evaluate $\boldsymbol{Y}$ instead of $\boldsymbol{U}$. As discussed by Hauke and Hughes [15], $\boldsymbol{U}$ is often not the best choice of state variables, particularly when the flow is nearly incompressible. For the calculations performed herein, the SUPG stabilized method was applied with linearly interpolated pressure-primitive variables which are discussed in detail by Whiting et al. [62]

$$\boldsymbol{Y} = \{\,Y_1 \quad Y_2 \quad Y_3 \quad Y_4 \quad Y_5\,\}^{\mathrm{T}} = \{\,p \quad u_1 \quad u_2 \quad u_3 \quad T\,\}^{\mathrm{T}}. \tag{37}$$

By inspecting (14)–(16) it is clear that all quantities appearing in (36) may be evaluated using (37).

To develop a numerical method, the weight functions ($\boldsymbol{W}$), the state variable vector ($\boldsymbol{Y}$), and its time derivative ($\boldsymbol{Y}_{,t}$) are expanded in terms of basis functions (typically piecewise polynomials); all calculations described herein were performed with a linear basis function. The extension of the quadratic and cubic basis can be done as well on the validated quadratic and cubic bases implementation of Whiting et al. [62]. The integrals in (36) are then evaluated using Gauss quadrature resulting in a system of non-linear ordinary differential equations which can be written as

$$\boldsymbol{M}\dot{\underline{\boldsymbol{Y}}} = \boldsymbol{N}(\underline{\boldsymbol{Y}}), \tag{38}$$

where the under bar is added to make clear that $\underline{\boldsymbol{Y}}$ is the vector of solution values at discrete points (spatially interpolated with the finite element basis functions) and $\dot{\underline{\boldsymbol{Y}}}$ are the time-derivative values at the same points. Finally, this system of non-linear ordinary differential equations are solved using a fourth order explicit Runge–Kutta time integrator with a lumped mass matrix.

4.1. The discontinuity capturing operator

Despite the success of the SUPG, it is well known to be insufficient for flows which contain discontinuities. For example, SUPG does not preclude overshooting and undershooting about sharp layers. Therefore, Hughes et al. [23]; Tezduyar and Park [55]; Hughes [19] suggested a simple technique for improving resolution of sharp layers while maintaining the optimal rate of convergence. The method adds an additional "discontinuity capturing term" (DC) which has a form similar to the streamline term, but acts in the direction of the solution gradient rather than in the direction of the stream line [23,55,19]. The dependence of this term on the solution gradient results in a discrete method, which is non-linear even if the original PDE is linear. This is of little consequence to the problems that are considered here, since the inherent flow non-linearity is more severe than the non-linearity introduced by this operator.

The discontinuity operator adds an additional term to the original variational formulation, (36), [46,47]. This term provides additional control over gradients in the discrete solution and considerably increases the robustness of the methodology. The DC operator needs to have the following properties: (i) in order to control oscillations, this operator should act in the direction of the gradient; (ii) for consistency, it should be proportional to the residual; (iii) for accuracy, it should quickly vanish in smooth regions of the solution. The term derived by Hughes [19] is of the form

$$\sum_{e=1}^{n_{\mathrm{el}}} \int_{\Omega^e} v^h \hat{\nabla}_\xi W^h \cdot [\tilde{\boldsymbol{A}}_0] \hat{\nabla}_\xi V^h \, \mathrm{d}\Omega, \tag{39}$$

here, $\hat{\nabla}_\xi$ is the generalized local-coordinate gradient operator and v^h is scalar discontinuity capturing factor of dimension reciprocal time, $[\tilde{\boldsymbol{A}}_0]$ is the conversion matrix from the conservative variables to the entropy variables [46,47] and $\boldsymbol{V}$ indicates the entropy variables described in Appendix A. The DC operator can be written more explicitly (for our choice of variables $\boldsymbol{Y}$) as

$$\sum_{e=1}^{n_{\mathrm{el}}} \int_{\Omega^e} v^h g^{ij} W^h_{,i} \cdot [\tilde{\boldsymbol{A}}_0] \boldsymbol{Y}_{,j} \, \mathrm{d}\Omega, \tag{40}$$

where $\boldsymbol{Y}$ is the pressure primitive variables described in (37) and g^{ij} is the inverse of the Jacobian of the mapping. The discontinuity factor v^h is defined as

$$v^h = \max\left\{0, \left[\frac{(\mathscr{L}\boldsymbol{Y} - \mathscr{S}) \cdot \tilde{\boldsymbol{A}}_0^{-1} (\mathscr{L}\boldsymbol{Y} - \mathscr{S})}{g^{ij} \boldsymbol{Y}_{,i} \cdot \boldsymbol{A}_0^{\mathrm{DC}} \boldsymbol{Y}_{,j}}\right]^{\frac{1}{2}} - \left[\frac{(\mathscr{L}\boldsymbol{Y} - \mathscr{S}) \cdot \tilde{\boldsymbol{\tau}} (\mathscr{L}\boldsymbol{Y} - \mathscr{S})}{g^{ij} \boldsymbol{Y}_{,i} \cdot \boldsymbol{A}_0^{\mathrm{DC}} \boldsymbol{Y}_{,j}}\right]\right\}, \tag{41}$$

where

$$\boldsymbol{A}_0^{\mathrm{DC}} = \boldsymbol{V}_{,Y}^{\mathrm{T}} \tilde{\boldsymbol{A}}_0 \boldsymbol{V}_{,Y} = \boldsymbol{V}_{,Y}^{\mathrm{T}} \boldsymbol{A}_0. \tag{42}$$

From the above description of DC operator, one can see that this term acts in the direction of the solution gradient but also dependent on the residual of the solution and the gradient itself. Therefore in the smooth regions where the residual is small, the operators are small and have little effect on solution. On the other hand in non-smooth regions the operators are larger and have strong control over the gradients of the solution. Hence, the non-linear DC operator provides good control in the regions of the flow where there are strong gradients and vanishes in smooth regions.

4.2. Finite element formulation for the level set method

Eqs. (21) and (29) can be represented by a single scalar advection equation of the form

$$\frac{\partial \theta}{\partial t} + \boldsymbol{a} \cdot \nabla \theta = S. \tag{43}$$

In case of the level set equation, $\theta = \phi$, $\boldsymbol{a} = \boldsymbol{u}$ and the forcing function S is zero. On the other hand, in the case of the re-distancing equation, $\theta = d$, $\boldsymbol{a} = \boldsymbol{v}$, and S is given by (28). This section presents the general finite element formulation for the scalar advection equation, (43). The solution strategy for solving this equation is similar to that used for the equations of motion, as discussed in Section 4.

Again, the spatial discretization is performed using the finite element method (FEM), and the finite element approximation spaces, namely the solution and the weight function space, are the scalar counterparts of the ones defined previously in Section 4. In keeping with the approach of the FEM described previously, we write (21) in residual form. To derive the weak form of the residual form, (21) is multiplied by a smooth weighting function, ψ, belonging to a space of functions $\psi \in \Psi_h$ (the scalar counterpart of the vector space defined in Section 4). The product is then integrated over a spatial domain. As the equation is solved in the convective form, we do not integrate by parts thus there are no boundary integrals. The resulting weak form is to find $\theta \in \Theta_h$ (the scalar solution space) such that

$$\int_{\Omega}(\psi\theta_{,t}+\psi a_i\theta_{,i}-\psi S)\,\mathrm{d}\Omega+\sum_{e=1}^{n_{\mathrm{el}}}\int_{\Omega_e}\left\{\hat{\mathscr{L}}^{\mathrm{T}}\psi\tau(\theta_{,t}+a_i\theta_{,i}-S)\right\}\mathrm{d}x=0 \tag{44}$$

for all $\psi\in\Psi_h$. Here τ is the stabilization parameter, defined as

$$\tau=\frac{C}{\sqrt{c_1/\Delta t^2+c_2u_ig_{ij}u_j}}, \tag{45}$$

where C, c_1, and c_2 are defined based on the one-dimensional, linear advection–diffusion equation using a linear finite element basis and $g_{ij}=\xi_{k,i}\xi_{k,j}$ is the covariant metric tensor related to the mapping from global to element coordinates. As before, by replacing $\hat{\mathscr{L}}^{\mathrm{T}}$ by $\hat{\mathscr{L}}^{\mathrm{adv}}$ (for the scalar equation $\hat{\mathscr{L}}^{\mathrm{adv}}=a_i\frac{\partial}{\partial x_i}$), we obtain the SUPG (streamline upwind Petrov–Galerkin) stabilization method [7]. Next, the weight functions (ψ), the solution variable (θ), and its time derivative ($\theta_{,t}$) are expanded in terms of linear basis functions. The integrals are then evaluated using Gauss quadrature resulting in a system of ordinary differential equations which can be written as

$$\boldsymbol{M}\dot{\theta}=\boldsymbol{N}(\theta). \tag{46}$$

The system of ODE's (linear, when $\theta=\phi$, and non-linear when $\theta=d$) is converted to an algebraic system by introducing an explicit time integrator (4th order Runge–Kutta for $\theta=\phi$, and forward Euler for $\theta=d$). Then, the two coupled systems (flow and scalar, i.e., (46) and (38)) are solved successively one after the other within each time step. During which, the interface is convected with the local flow speed, which, as mentioned before, distorts the distance function. As discussed earlier, this distance function is restored by the solution of (29) via a finite element discretization, as discussed in Section 4.2. During this re-distancing step, additional care is taken to restrict the interface from moving. To constrain the interface, we implemented a strategy proposed by Sussman et al. [51,50,48] for a finite difference method. The principle behind the constraint calculations is to enforce the volume filled by each phase in an element to remain constant when the re-distance step is applied [34], which is an extension of the method proposed by Sussman et al. [51] to FEM methods.

4.3. Ghost fluid method

Although Eulerian schemes work well for most compressible flows, they may admit spurious non-physical oscillations near the material interfaces [3]. Fedkiw et al. [11] proposed a new numerical method for treating interfaces in Eulerian schemes that maintains a Heaviside profile of the density with no numerical smearing. They also used the level set function to track the interface in their work. In addition, they used ghost cells (called ghost nodes in their finite difference frame work) to prevent the smearing of the density across the interface. The motivation for their method stems from the fact that the non-physical oscillations encountered by Eulerian schemes across the material interface are due to the radical change in the equation of state across the material interface. On the other hand, Lagrangian schemes do not smear the density profile, and it is clear which equation of state is valid at each location. However, Lagrangian schemes have problems when subjected to large deformations. A good summary of both Eulerian and Lagrangian schemes is given by Benson [3]. The original method proposed by Fedkiw et al. [11] tracks the interface with the level set function which gives the exact sub cell interface location. At the interface, they solved an approximate Riemann problem similar to the methods in Fedkiw et al. [12] and Coquel and Saurel [9].

The approach used in this work is based on the method proposed by Fedkiw et al. [11]. The ghost fluid method previously developed for finite difference schemes was appropriately modified for our FEM formulations. In our method we used the level set function to keep track of the interface. The zero level set represents the location of the interface as discussed in previous section, positive level sets representing the heavier fluid (i.e., the liquid) and the negative values representing the lighter fluid (i.e., the gas). The fluid satisfies a different equation of state on each side of the interface. A clear demarcation can be made from the exact representation of the interface location by zeroth level set. Next, we define a ghost element in addition to the existing element for every element which is intersected by an interface. The ghost elements which contain the interface have the mass, momentum and energy of both the fluids. This is done by evaluating the integrals in (36) accordingly.

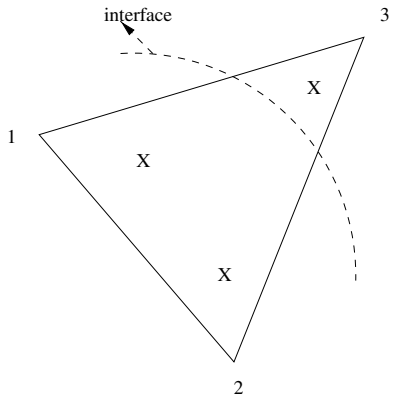

Fig. 1. A typical triangular element containing an interface.

Fig. 1 shows a typical two-dimensional triangular element which is intersected by the interface. For example, assume that the nodes 1, 2, are in the liquid phase, where as node 3 lies inside the gas phase. Hence, for this element, we define a ghost element containing a ghost fluid. The integrals over this element are evaluated first assuming that the whole element is occupied by the liquid phase and then by assuming it is occupied by the gas phase. While building the nodal contributions to both the right hand side and the left hand side, a choice is made between the liquid or gas integral depending on whether the node lies in liquid or gas phase. Hence, in the above example, while evaluating the local residual at node 1, we choose the liquid integral, while on the other hand, the local residual at node 3 is evaluated based on the integral evaluation for gas phase.

The method can be further explained by a simple 1-D example. Consider the simple 1-D domain shown in Fig. 2. The domain is divided into three elements, and the second element is intersected by the interface. Let us assume that the region to the left of the interface contains the liquid phase and the region to the right contains the gas phase. The figure shows both the local and the global node numbering. The finite element discretization leads to an ordinary differential equation,

$$\sum_{B=1}^{\mathrm{nel}_{\mathrm{node}}} \boldsymbol{W}_B \boldsymbol{G}_B = 0. \tag{47}$$

This implies that, if the weight functions are chosen to be arbitrary, then $\boldsymbol{G}_B = 0$, where $\boldsymbol{G}_B$ is obtained by assembling the local $\boldsymbol{G}^e_b$. Note the 'B' indicates the global node numbering, the subscript 'b' indicates the local node number. The superscript 'e' denotes the element number. For the above 1-D example, the global assembly operation will be defined as follows:

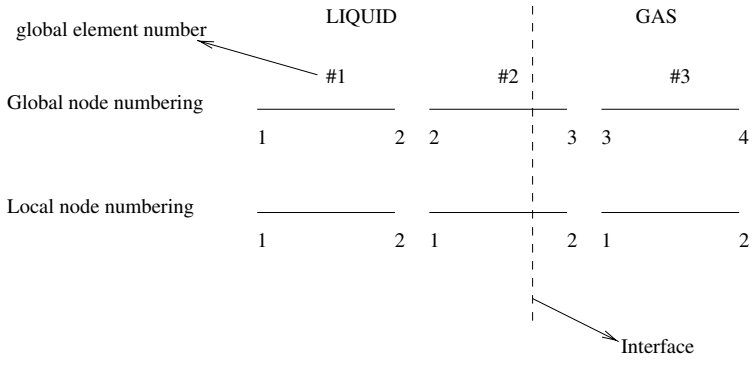

Fig. 2. A 1-D example of global and local numbering.

$$\boldsymbol{G}_1 = \boldsymbol{G}_1^1, \tag{48}$$

$$\boldsymbol{G}_2 = \boldsymbol{G}_2^1 + \boldsymbol{G}_1^2, \tag{49}$$

$$\boldsymbol{G}_3 = \boldsymbol{G}_2^3 + \boldsymbol{G}_1^3. \tag{50}$$

The element level residual $\boldsymbol{G}_b^e$ can be defined as

$$\boldsymbol{G}_b^e = \int_{\Omega^e} g_b^e(\tilde{\xi})\,\mathrm{d}\Omega^e = \sum_{k=1}^{\mathrm{nqpt}} g_b^e(\tilde{\xi}_k)\cdot \boldsymbol{W}_k, \tag{51}$$

where

$$g_b^e(\tilde{\xi}_k) = \sum_{b=1}^{\mathrm{nenl}} g^e(\tilde{\xi}_k)\cdot N_b \ (\text{or } N_{b,i}). \tag{52}$$

In the above equations, 'nqpt' denotes the number of Gaussian quadrature points and the 'nenl' indicates the number of element nodes. The ghost fluid method calculates $g^e(\tilde{\xi}_k)$ twice for the elements that contain the interface. Once assuming the whole element is occupied by the liquid phase and once by assuming this occupied by the gas. While evaluating $g_b^e(\tilde{\xi}_k)$, depending upon whether node b resides in the liquid phase or gas phase, the correct $g^e(\tilde{\xi}_k)$ is selected. In essence the method assumes a ghost fluid in all the elements that are cut by an interface. This ghost fluid behaves as a pure liquid for the nodes that are in the liquid phase and behaves as a pure gas when seen from the nodes that are in gas phase. In this way, we have continuous pressure and velocity fields while avoiding the numerical dissipation due to different phasic equations of state. The resulting numerical method allows us to keep the density profile from smearing out, while still preserving the robustness of the numerical method.

5. Numerical results and discussion

Although the focus of the present work was a numerical simulation of the hydrodynamics of an imploding air bubble, it would be foolhardy to apply the new method described heretofore to such a complex problem without first validating it against some simple, well understood problems. This is the motivation for the simulations presented in Sections 5.1 and 5.2. In particular, we first demonstrate that the new algorithm can: (i) track an interface accurately; (ii) properly represents compressible gas dynamics; (iii) capture shocks. More comprehensive and complex three-dimensional studies applying similar three-dimensional finite element formulation with level sets for the simulation of incompressible bubble dynamics can be found in Nagrath et al. [34].

5.1. Simple advection of a cylindrical bubble

To demonstrate the validity of the numerical algorithm, a simple test problem of advecting a 2-D cylindrical air bubble through a rectangular domain was considered. The ratio of density of the liquid to gas was, 1000 (i.e., water/air). The liquid was flowing with a constant uniform velocity of 1 mm/s in the vertical direction and the buoyancy force was assumed to be zero (i.e., gravity was zero). The effect of surface tension was not considered here. Hence, the bubble should simply advect through the domain with the velocity of the liquid. The domain and the initial position of the bubble are shown in Fig. 3. The computational domain dimensions are: $-2.0\ \mathrm{mm} \leqslant x \leqslant 2.0\ \mathrm{mm}$, $-2.0\ \mathrm{mm} \leqslant y \leqslant 8.0\ \mathrm{mm}$, and $0\ \mathrm{mm} \leqslant z \leqslant 1\ \mathrm{mm}$, and the mesh consists of 640 hexahedral elements ($16 \times 40 \times 1$). Periodic boundary conditions are applied in x- and z-directions. A uniform velocity of 1 mm/s was specified at the inlet and a constant pressure boundary condition was applied at the exit of the domain. The bubble radius was 1.25 mm, and the bottom of the bubble is positioned at -1.25 mm. The motion of the bubble through the domain is shown in Fig. 4. As the fluid velocity is 1 mm/s, the bubble is expected to travel a distance of 4 mm at the end of 4 s. The numerical results show that the bubble traveled 4 mm in 4 s as measured by the displacement of bottom of the bubble in vertical direction. The percentage error in the calculated mass of the bubble at the end of 4 s is 0.0049. Clearly, the bubble is

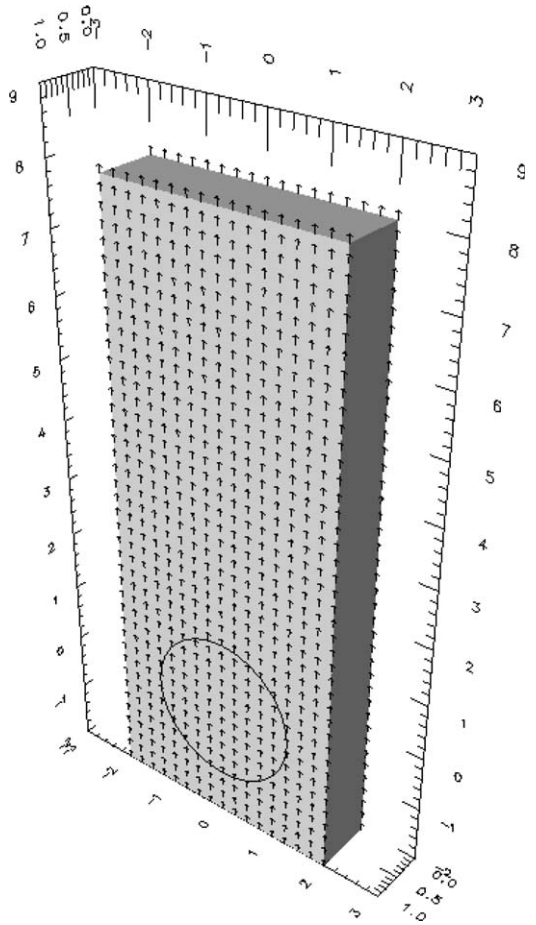

Fig. 3. The computational domain and bubble position at $t = 0$.

advected with the right fluid velocity and the shape of the bubble is preserved along with the conservation of mass of the bubble.

5.2. Two-phase shock tube problem

The next test case is similar to the problem investigated by Fedkiw et al. [11] and Wardlaw [60]. In this problem, we consider a one-dimensional shock tube of length 10 m in x-direction, with the interface located at 5 m. The initial conditions for pressure and velocity are shown in Figs. 5 and 6, respectively. The location of the interface is marked with a '*' in the plots. To the left of the interface is gas, and to the right is liquid. The gas phase was assumed to be an ideal gas and the liquid phase was described by a linear equation of state. The initial conditions on the immediate left and right side of the interface are: $\rho_l = 1$ kg/m^3, $\rho_r = 1000$ kg/m^3, $p_l = 1.0 \times 10^5$ Pa, $p_r = 1.0 \times 10^5$ Pa, and $u_l = u_r = 0$ m/s. In addition, both liquid and gas phases have a shock located at 0.94 m, and at 9.6 m, respectively. The shock in the gas phase is moving to the right and the conditions behind the shock are: $\rho = 8.27$ kg/m^3, $p = 1.0 \times 10^7$ Pa, and $u = 2949.97$ m/s. On the other hand, the shock in the liquid phase is moving to the left, and the conditions behind the shock are: $\rho = 1004.13$ kg/m^3, $p = 1.0 \times 10^7$ Pa, and $u = -6.38$ m/s.

With time, the two shocks move towards the interface, however the faster traveling shock in the gas phase strikes the interface first and sends a reflected wave back into the gas, and transmits a shock into the liquid phase. This newly generated shock merges with the existing shock in liquid phase. The solution at $t = 0.003$ s obtained using our numerical method is shown in Figs. 7–9. At this time, the interface has moved

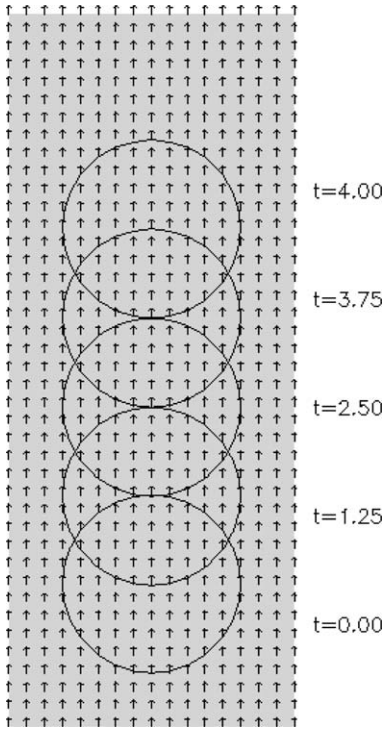

Fig. 4. Bubble position at various time instants.

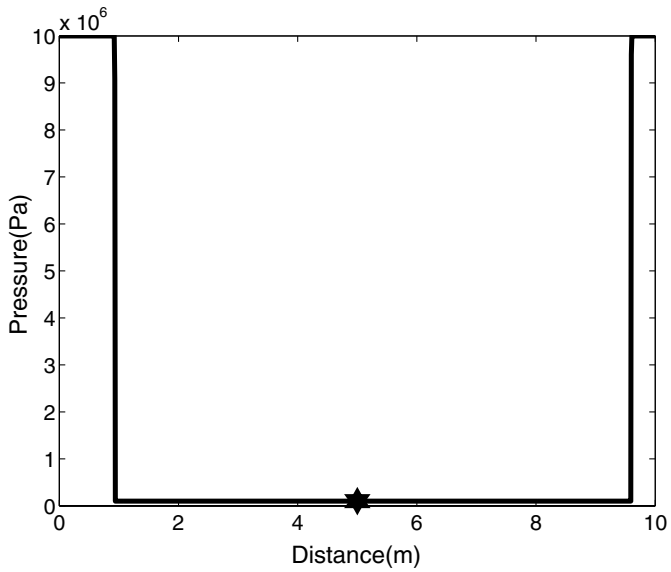

Fig. 5. Initial pressure distribution.

to 5.031 m, and there is a shock wave moving to the left in the gas phase and a shock wave moving to the right in the liquid phase. At $t = 0.0003$ s the shock in the gas phase is located at 1.211 m and the pressure behind the shock is 2.96×10^5 Pa. At this time, the shock in the liquid phase is located at 7.347 m and the pressure behind the shock is 4.808×10^7 Pa. The computed results are in excellent agreement with the results presented by Fedkiw et al. [11] and Wardlaw [60] for the shock strength and location in each phase.

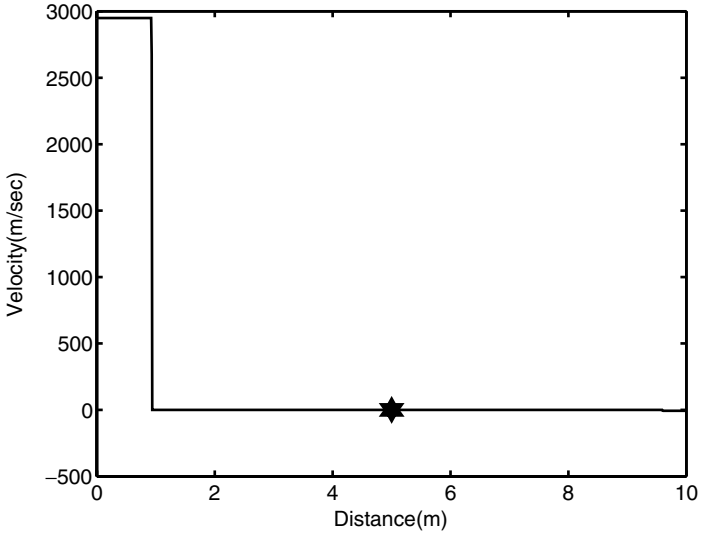

Fig. 6. Initial velocity distribution.

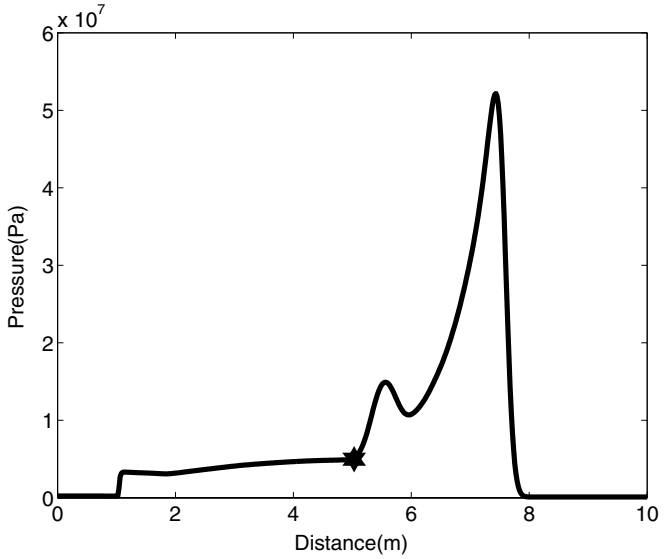

Fig. 7. Pressure distribution at $t = 0.003$ s.

5.3. Imploding air bubble in water

Let us now consider the 3-D hydrodynamic shock (i.e., HYDRO) code analysis of an imploding air bubble which is initially spherical. The primary purpose of this study was to study bubble implosions using a full 3-D transient DNS solution and to appraise any shape and interfacial instabilities in the fully non-linear analysis. For simplicity, the perfect gas law for gas phase and a linear equation of state for liquid phase were used for both the Rayleigh model and hydrodynamic shock code simulations, even though it is known that a more sophisticated equation of state is required for realistic simulations of sonoluminescence [33] and sonofusion [36].

We consider a spherical air bubble which was initially at atmospheric pressure and was being compressed by the surrounding pressurized liquid at 100 atmospheres. The initial radius of the bubble was 10 μm, and the

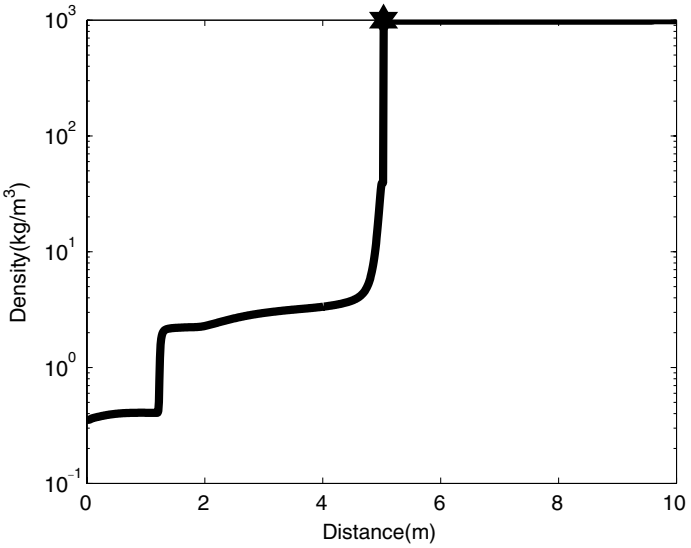

Fig. 8. Density distribution at $t = 0.003$ s.

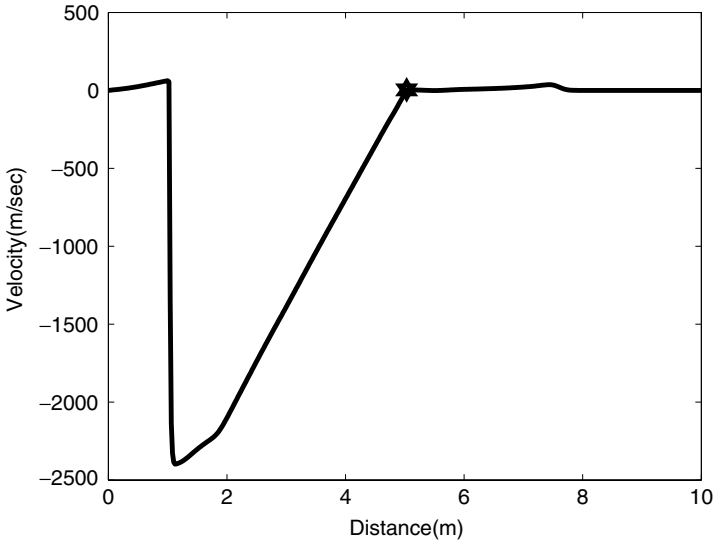

Fig. 9. Velocity distribution at $t = 0.003$ s.

radius of the computational domain was 50 μm. The density of the water and air were taken to be 1000 and 1.226 kg/m^3, respectively. The viscosity of liquid phase was taken as 3.5×10^{-1} kg/m s, and the viscosity of the air to be, 3.58×10^{-3} kg/m s. The initial conditions chosen are typical of the parameters encountered in prior sonoluminescence and cavitation studies. To save computational time, we derived the initial conditions analytically to start the simulations. In particular, we solved the equations presented in Section 2 until $t = 0.06$ μs, and prescribed the resultant pressure and the velocity as the initial conditions to start the DNS. The usage of these initial conditions saves computational time, but is not a requirement to start the calculations. The rationale behind choosing to solve the Rayleigh equation only up to a particular time is so, we do not exceed a reasonable Mach number for the interface velocity ($\frac{|\dot{R}|}{C_g}$). For the particular choice of $t = 0.06$ μs, the radial interface velocity is 80.77 m/s, hence the gas Mach number was approximately 0.3. At this instance, the predicted value of the radius of bubble was 7.95 μm. Spherically symmetry was valid at this instance and indeed until much longer in time, as confirmed in our numerical results.

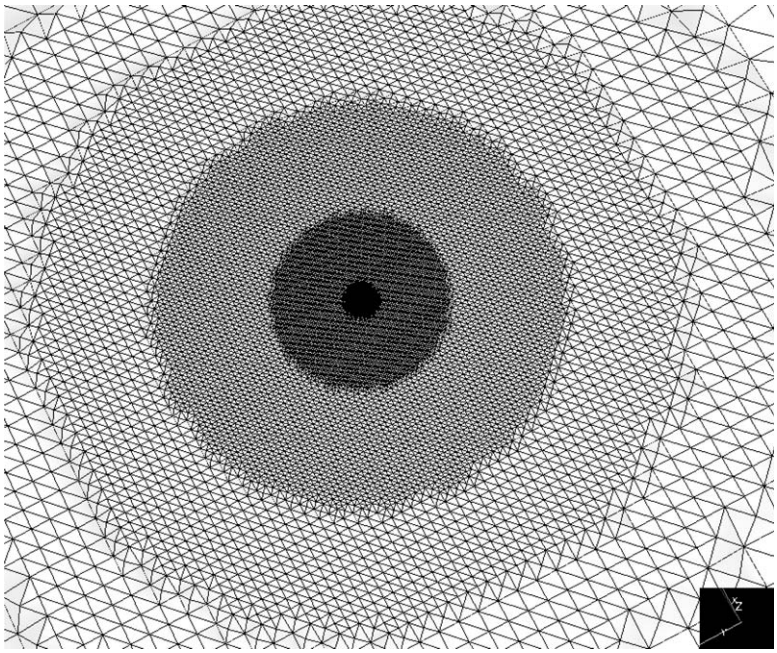

Fig. 10. Mesh used for the simulation bubble implosion.

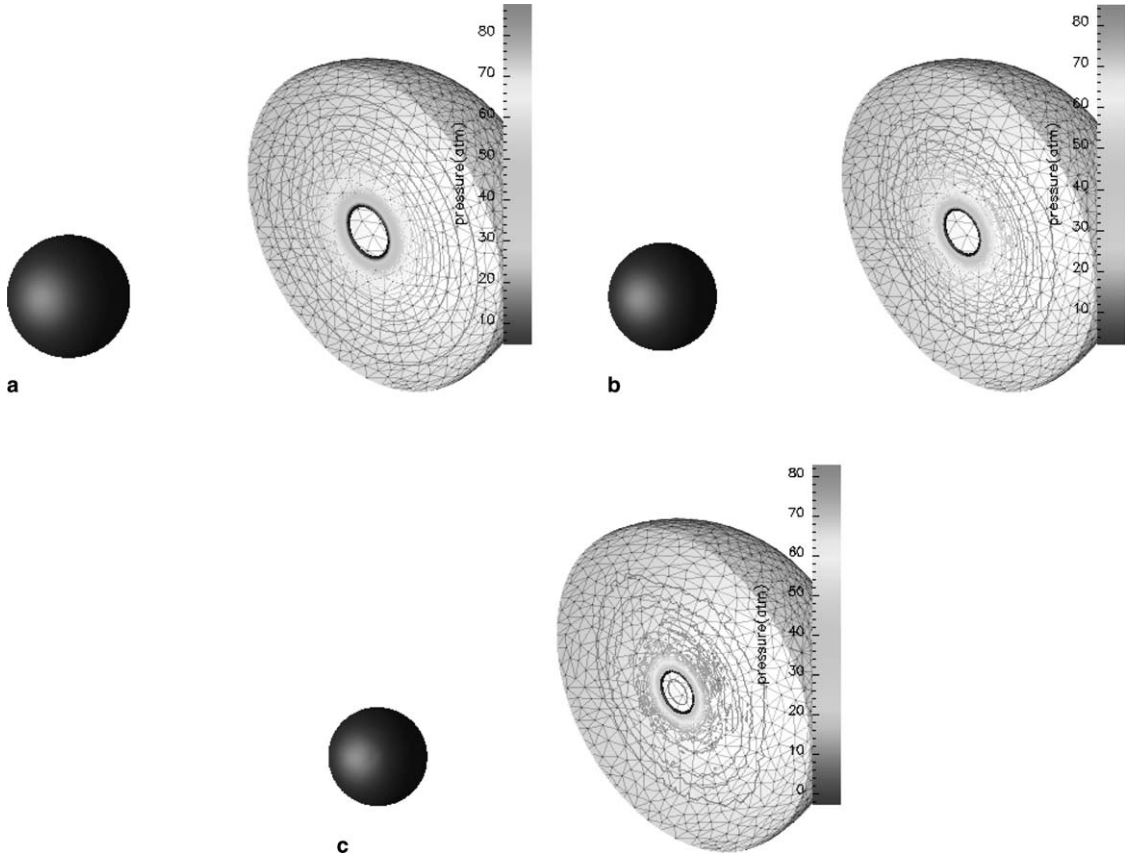

Fig. 11. Early stages of bubble implosion: (a) $t = 0.06$ μs; (b) $t = 0.07$ μs; (c) $t = 0.075$ μs.

The non-uniform mesh used for the simulation is shown in Fig. 10. This figure shows a plane view of the three-dimensional mesh. One can see from the figure, various levels of mesh refinement. The inner most fine mesh affords adequate resolution of the near-singularity when the converging shock collapses at the center. The next level of finer mesh resolves the interface and the vicinity of the shock accurately (a series of grid refinements were done to verify the local accuracy needs). The early stages of the bubble implosion are shown in Fig. 11. A plane is cut through the center of the domain and pressure contours are displayed on this plane. The solid black line on the contour plots represents the interface location on this plane. Also shown to the left in each sub-figure is the three-dimensional bubble to better show the changes in bubble size and shape. The initial pressure profile imposed to start the numerical calculations is shown in Fig. 11(a). During the initial stages of the implosion, the inertial motion of the liquid compresses the gas bubble. As a result the pressure inside the bubble begins to increase. Fig. 11(a)–(c) clearly shows the decrease in the size of the bubble. We note that during this early stage of the bubble collapse, the bubble remains spherical, and the pressure varies smoothly inside the liquid phase. Fig. 12 shows later stages of the implosion, and Fig. 13 shows the variation of pressure along the radius of the bubble at various times during the early stages of implosion. In this time frame, the bubble continues to decrease in the size and a pressure front in liquid phase is approaching the interface. As it moves towards the interface, the intensity increases due to the converging geometry. The pressure starts to build at the interface, and due to volumetric compression an increase in the gas pressure inside the air bubble can be observed. However, the pressure is still essentially uniform inside the air bubble. With time a shock wave develops. At $t = 0.091$ μs (Fig. 13), a shock is forming near the interface. Comparing Fig. 12(a)–(c), one can also observe that the bubble is also beginning to deviate from spherical shape. The

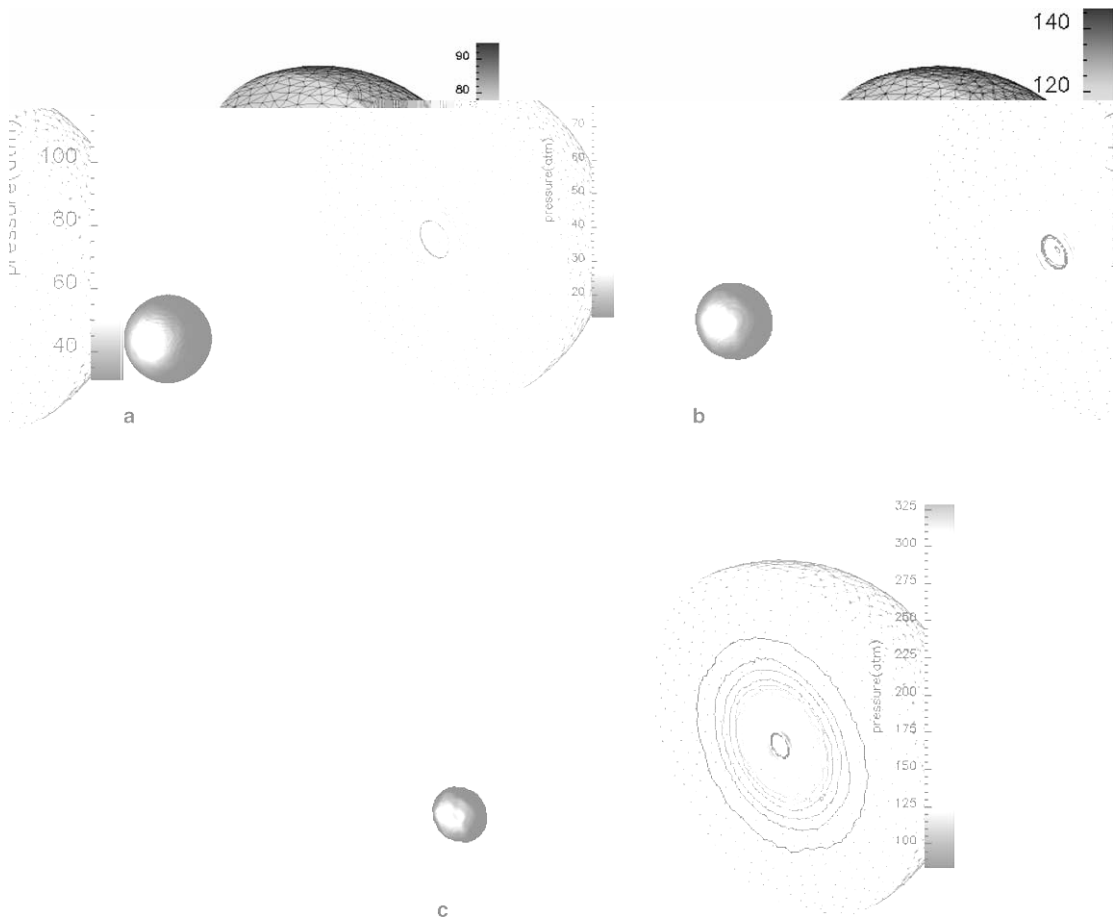

Fig. 12. Collapsing bubble: (a) $t = 0.08$ μs; (b) $t = 0.085$ μs; (c) $t = 0.090$ μs.

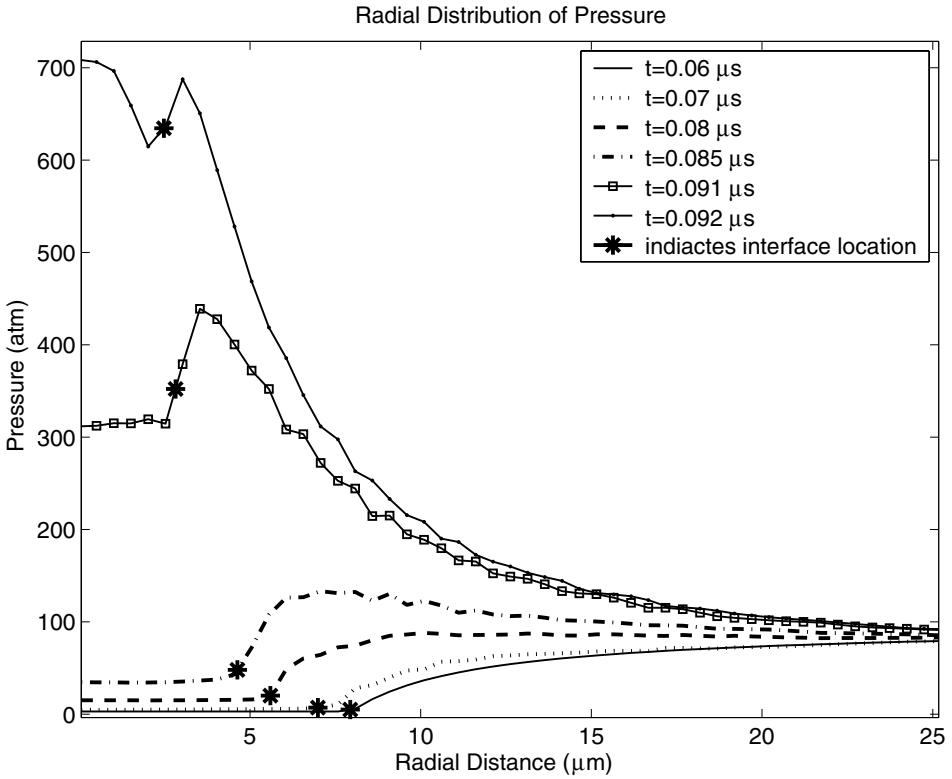

Fig. 13. Development of a shock in the gas.

collapse of the shock is seen in Fig. 14. In these figures, in addition to the actual bubble, a zoomed-in view of the bubble is also presented to show the deformed ellipsoidal shape more clearly. Also in this figure, the pressure distribution inside the gas phase is shown. At time $t = 0.092$ μs, the shock at the interface is moving into the gas phase, Figs. 14(a) and 13, and the bubble is collapsing rapidly. As the bubble collapses, the spherically convergent gas shock becomes much stronger and, as will be discussed subsequently, the peak pressure inside the gas bubble is on the order of 10^4 atmospheres. In addition, the interface velocity increases due to spherical convergence.

During the implosion, the bubble is compressed and the gas inside the bubble accelerates. The velocity distribution and the interface configuration are shown for three different planes in Figs. 17–19. These figures display the velocity vectors in the vicinity of the bubble along with the interface indicated by the dark line. The region focused in on in each sub-figure varies, as we want to show the distributions around the interface, the location of which is constantly changing. The density of the vectors also vary as the mesh size varies in those regions. The fluid moves inward until $t = 0.095$ μs (Figs. 17–19). Fig. 15(a) shows the instant of the shock collapse at the center of the bubble at 0.095 μs. At this instant the air is predicted to be compressed to a thousand times normal density, however, the perfect gas law which was used in the study is no longer valid at these extreme conditions. After the spherical shock impacts on itself at the center of the bubble, we can see from Figs. 17(d), 18(d), and 19(d), that the fluid inside the bubble reverses its direction and starts moving outward.

Figs. 20–22 display the velocity, pressure, and temperature profiles along with the temporal variation of the effective bubble radius. In each sub-plot, the velocity, pressure, and temperature are plotted along the x, y, and z axis. Figs. 20(a), 21(a) and 22(a) shows that the fluid moved inward until $t = 0.095$ μs. Also from the figures, it can be observed the velocity is almost linear inside the gas phase. The pressure profiles shown in Figs. 20(b), 21(b) and 22(b) depicts the converging shock as well as the diverging rarefaction wave, where the interface location is marked by '*'. Interestingly, in the later stages of implosion ($t \geqslant 0.093$ μs), the pressure inside

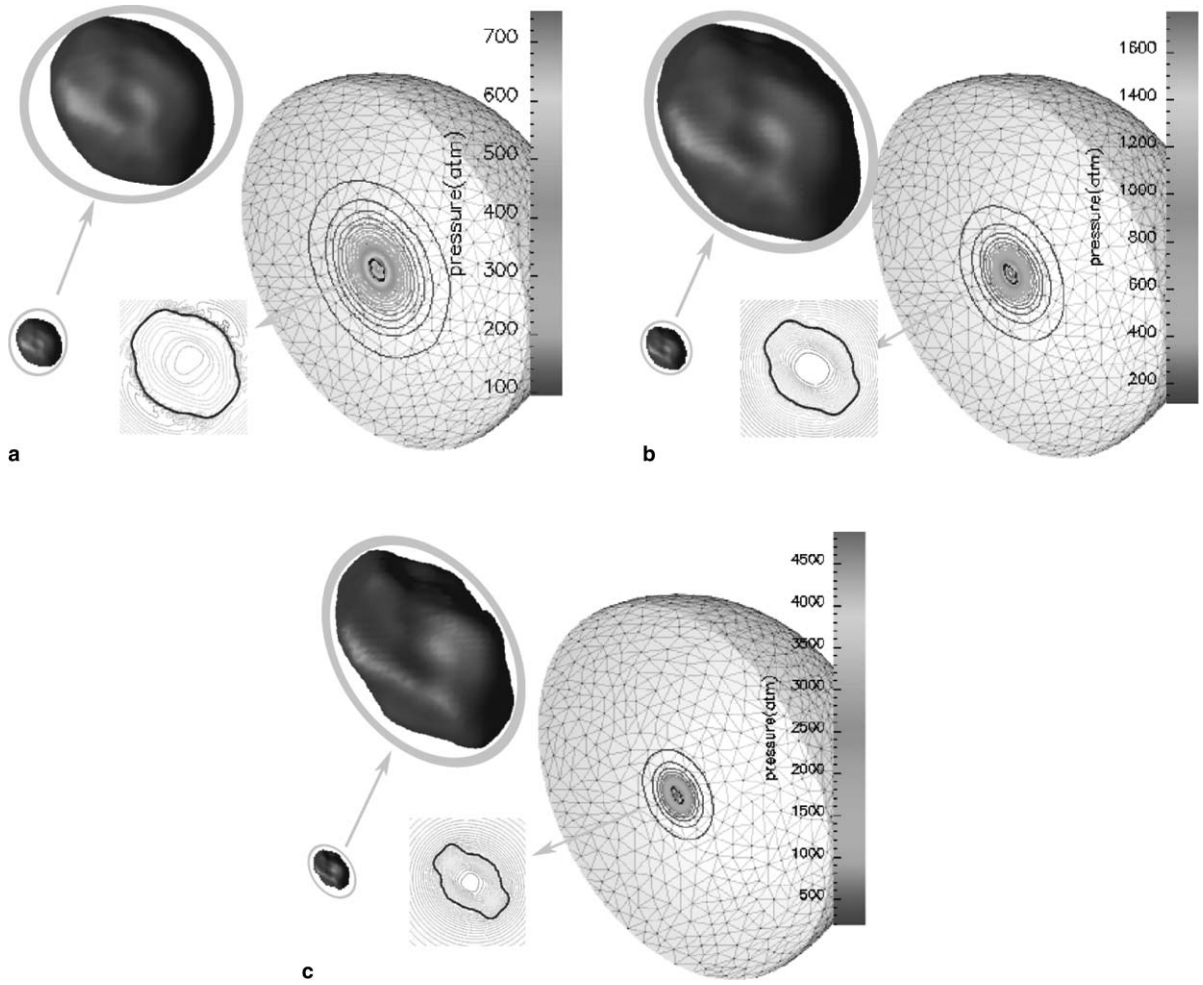

Fig. 14. Collapsing shock: (a) $t = 0.092$ μs; (b) $t = 0.093$ μs; (c) $t = 0.094$ μs.

the gas phase is almost uniform. This is due to the relatively high speed of sound in the compressed air and the radius of the bubble being quite small at these instants. The gas pressures attained at the instant of shock collapse is on the order of 10^4 atmospheres, which is an increase of two orders of magnitude over the driving pressure in the liquid. Figs. 20(c), 21(c), and 22(c) shows rather high temperatures near the center of the bubble during the implosion. The reflection of the convergent shock from the center creates a spherically divergent shock. Fig. 15(b) shows the rarefaction wave moving away from the center, and at this instant the bubble is still collapsing. However, the relatively large pressures and temperatures decrease rapidly behind the shock due to hydrodynamic expansion. Once the reflecting shock moving outward crosses the interface (Fig. 15(c)), the bubble stops collapsing and starts rebounding. Fig. 16 shows the rebounding bubble after collapse. It can be noted that Fig. 16(b) and (c) shows that the expanding bubble is regaining its spherical shape.

5.3.1. Hydrodynamics of collapse

Although we have stated that the bubble is still collapsing from $t = 0.095$ μs to $t = 0.096$ μs, this is not obvious from Fig. 15(a) and (b). However, this becomes clear if we take a look at the temporal variation of the radius. The temporal variation of the effective bubble radius was plotted along the three different axis and compared with the analytical predictions based on Rayleigh–Plesset model predictions for a spherical bubble in Fig. 23. This figure shows that during this period of time the size of the bubble measured along x and z axis

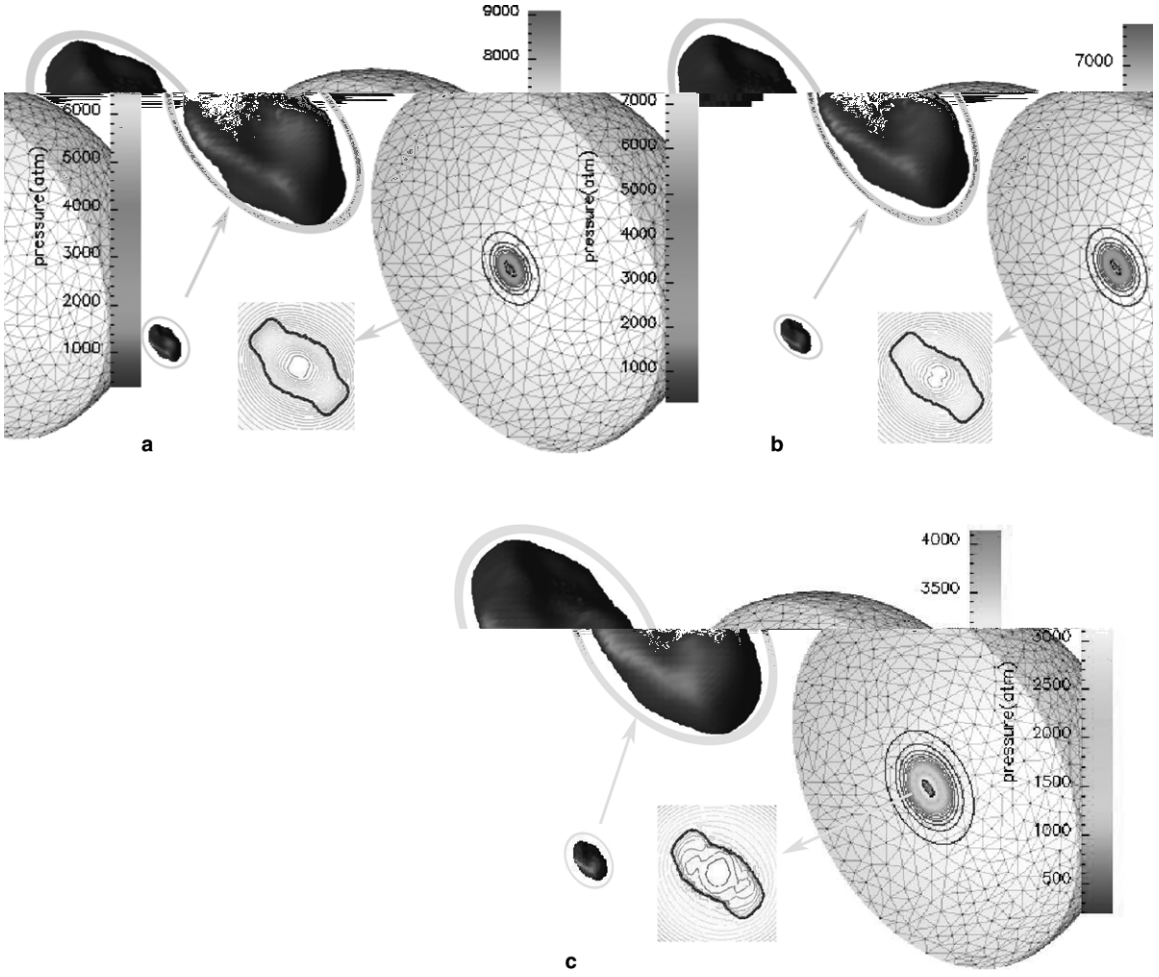

Fig. 15. Shock collapse and rebound: (a) $t = 0.095$ μs; (b) $t = 0.096$ μs; (c) $t = 0.097$ μs.

is almost stagnant. On the other hand, the effective radius measured along y axis is still decreasing. At $t = 0.097$ μs, the outward moving shock crosses the bubble's interface, and the radius measured along y axis also starts decreasing (Fig. 21(d)). Thus, the effective bubble radius continues to decrease in size until the reflected shock wave crosses the bubble's interface.

As seen in Figs. 12–15, it is clear that the bubble is no longer spherical during the final stages of the implosion. Figs. 17–19 also show the non-spherical bubble shape in different planes. This is the first time, that 3-D DNS predictions of this phenomena have been documented. Weninger et al. [61] postulated the non-sphericity of a collapsing bubble during single bubble sonoluminescence (SBSL). They conclude that the observed long time decay of the angle dependent correlation is due to the refraction of the sonoluminescence (SL) photons by the interface of a non-spherical bubble. Their studies predicted that the dipole component in the broadband measurements is due to the asphericity of the collapse. Also, there is some direct experimental evidence showing non-spherical bubble shapes [65].

The asphericity of the bubble can be attributed to many factors, such as the inherent dynamic instability of contracting bubbles, the proximity of solid boundaries or free surfaces, and buoyancy effects [42]. The DNS results presented herein implies that the deviation from spherical shape is due to the excitation of non-spherical shape instability modes of the gas bubble during the violent collapse [64]. Brenner et al. [6] in their work on acoustic energy storage during SBSL, showed that the most easily excited instability modes of bubble are not spherically symmetric.

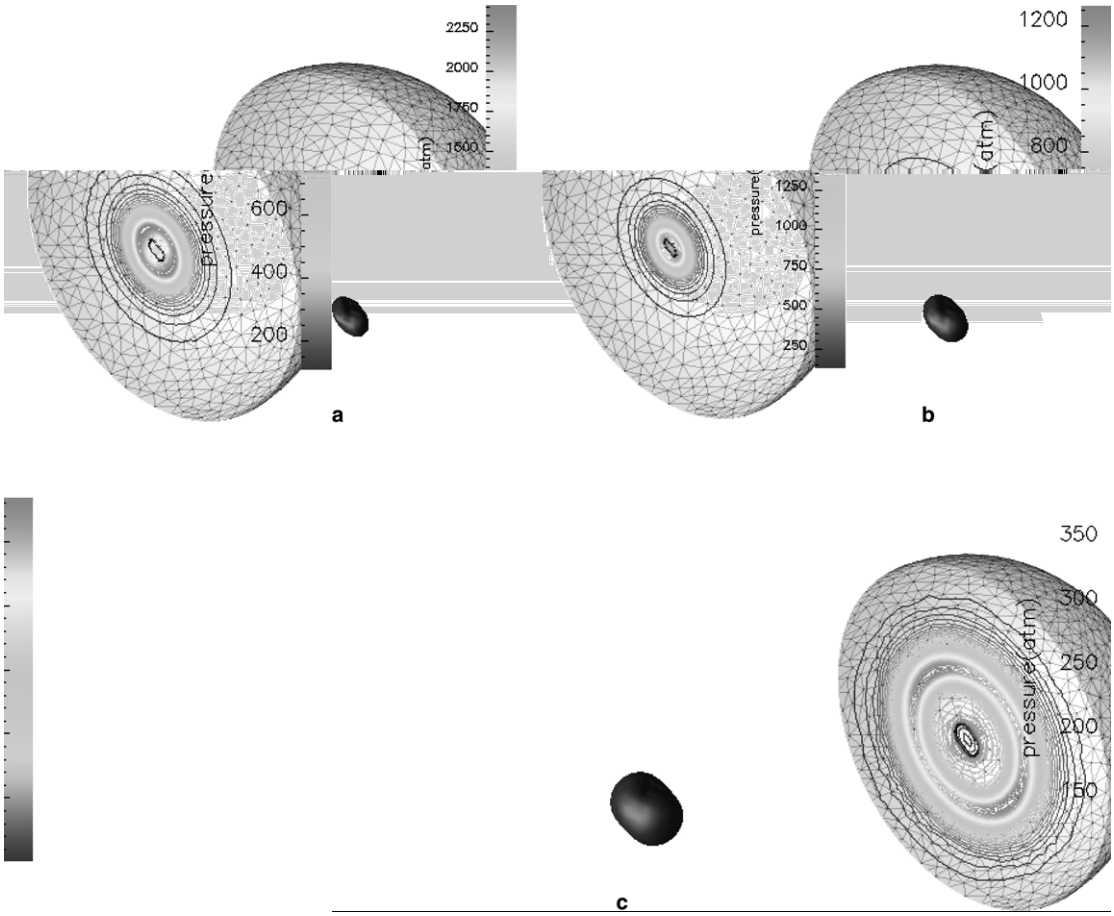

Fig. 16. Diverging shock and rebounding bubble: (a) $t = 0.098$ μs; (b) $t = 0.10$ μs; (c) $t = 0.15$ μs.

Moreover, the observance of an ellipsoidal-shaped bubble is expected as ellipticity is the leading order instability mode [61]. However, it was not clear in these prior studies, which order of the perturbation would be dominant during bubble collapse.

Hence, to further investigate the shape instabilities observed during the collapse stage, we performed an analysis on the growth of instabilities for a spherical interface. Plesset and Mitchelle [41] studied the problem of a spherical interface between two immiscible fluids of different densities for accelerated motions analogous to the planar interface studies by Taylor [52]. Later, Plesset and Prosperetti [42] further addressed the problems associated with the dynamics of non-spherical bubbles. The radius of the distorted bubble's interface can be represented as

$$r_s = R + \Sigma a_n Y_n, \tag{53}$$

where $R(t)$ is the instantaneous radius of the interface, Y_n is a spherical harmonic of order n, and the $a_n(t)$s are the amplitude of the spherical harmonic components of order n. The stability of the spherical interface can be determined based on whether the interface distortions of small amplitude grow or diminish. For small perturbations to the interface ($|a_n(t)| \ll R(t)$), the growth in amplitude of the perturbation is governed by [41,42]

$$\ddot{a_n} + \frac{3}{R}\dot{R}\dot{a_n} - Aa_n = 0, \tag{54}$$

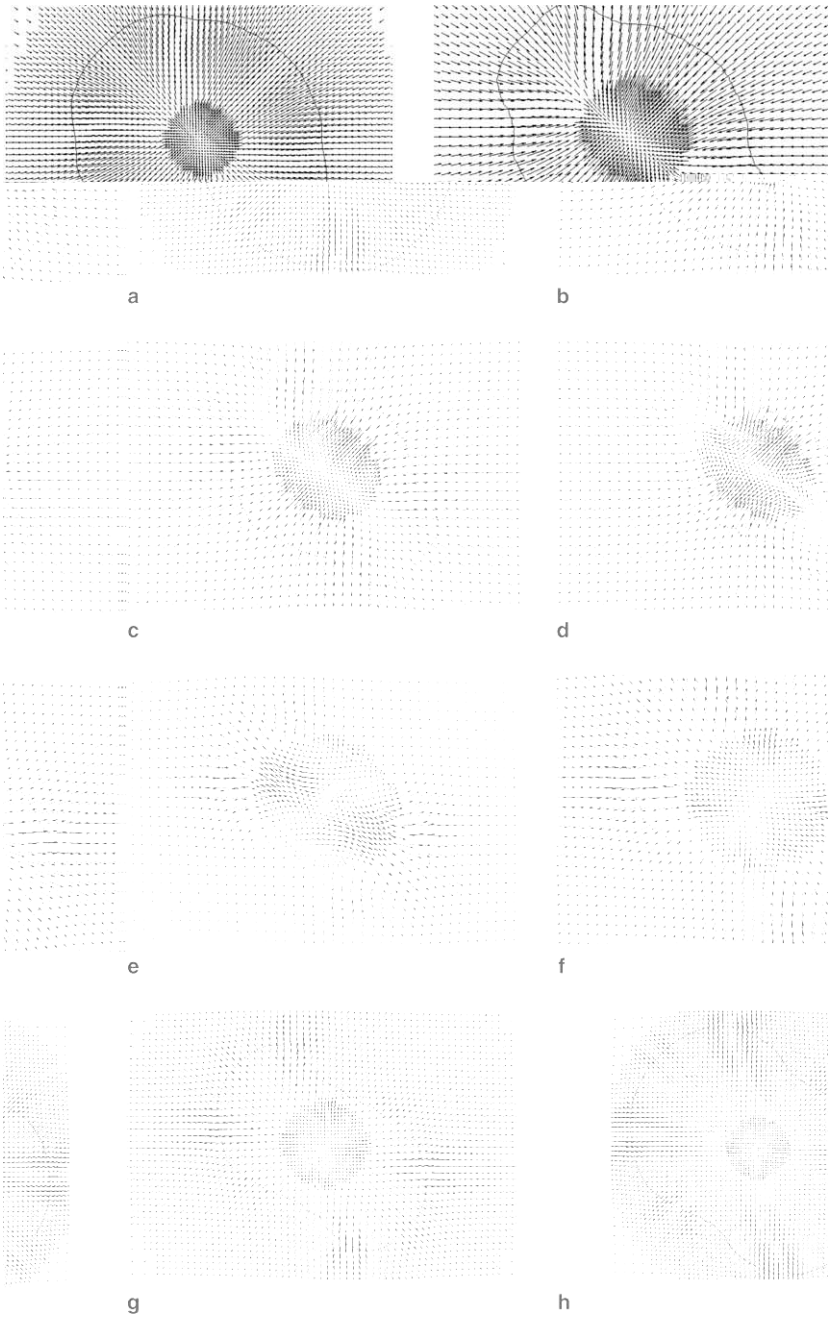

Fig. 17. Velocity distribution during the implosion displayed on a xy-plane: (a) $t = 0.090$ μs; (b) $t = 0.093$ μs; (c) $t = 0.094$ μs; (d) $t = 0.095$ μs; (e) $t = 0.096$ μs; (f) $t = 0.098$ μs; (g) $t = 0.10$ μs; (h) $t = 0.15$ μs.

where

$$A = \frac{[n(n-1)\rho_l - (n+1)(n+2)\rho_g]\ddot{R} - (n-1)n(n+1)(n+2)\sigma/R^2}{[n\rho_l + (n+1)\rho_g]R}. \tag{55}$$

Solving (54) together with (8) yields the evolution of amplitude with time. Fig. 24(a) shows the growth in amplitude (a_n) with time for different n. We can see that the instabilities do not grow until the final stages of bubble implosion. The variation of the distortion amplitude with mean bubble radius is shown in Fig. 24(b). One can observe that as the radius of the bubble decreases, the distortion amplitude may oscillate

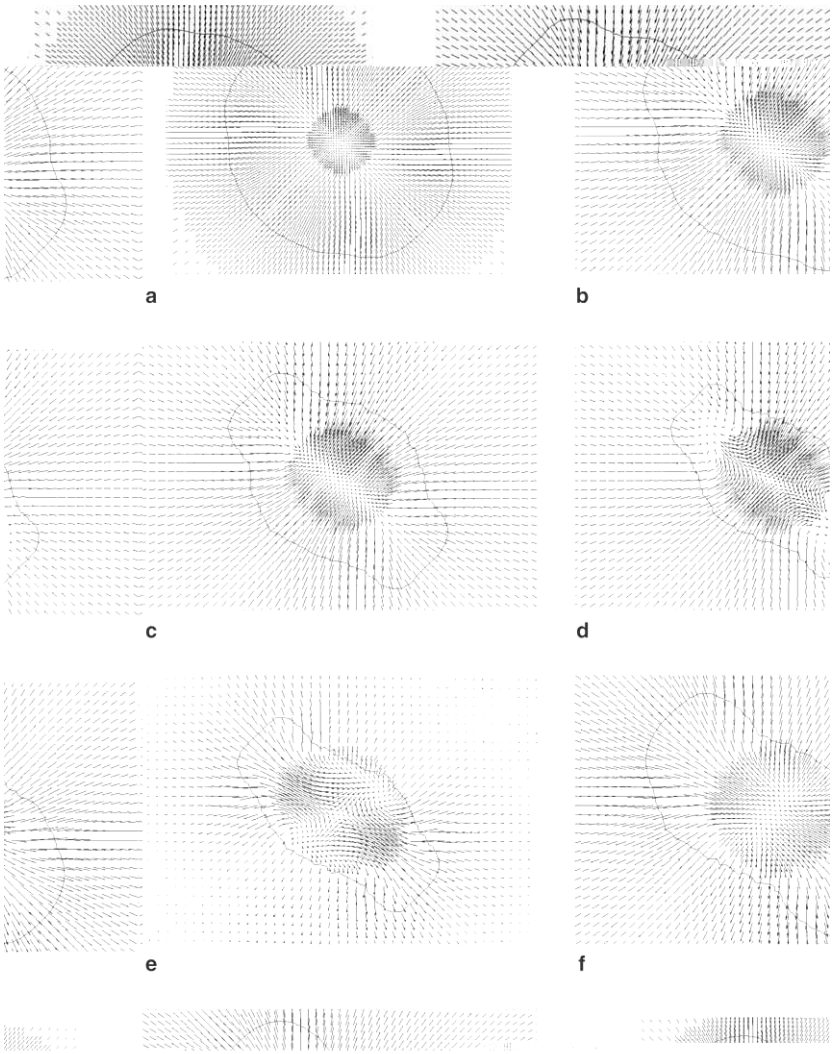

Fig. 18. Velocity distribution during the implosion displayed on a yz-plane: (a) $t = 0.090$ μs; (b) $t = 0.093$ μs; (c) $t = 0.094$ μs; (d) $t = 0.095$ μs; (e) $t = 0.096$ μs; (f) $t = 0.098$ μs; (g) $t = 0.10$ μs; (h) $t = 0.15$ μs.

in sign with increasing frequency and magnitude. From both Fig. 24(a) and (b) it can be noted that higher harmonics are excited. Hence the observance of shape instabilities in the DNS results is expected.

From the pressure distributions seen in Figs. 20(b), 21(b), and 22(b), one can see that the impact of the shock at the center, and the peak pressure, occurs at the same instant in all the directions. This is because the initial shock itself is spherically symmetric although the bubble is not. This is significant and is apparently the reason that previous spherically-symmetric predictions of the peak temperature and pressure conditions have been so successful [33,36].

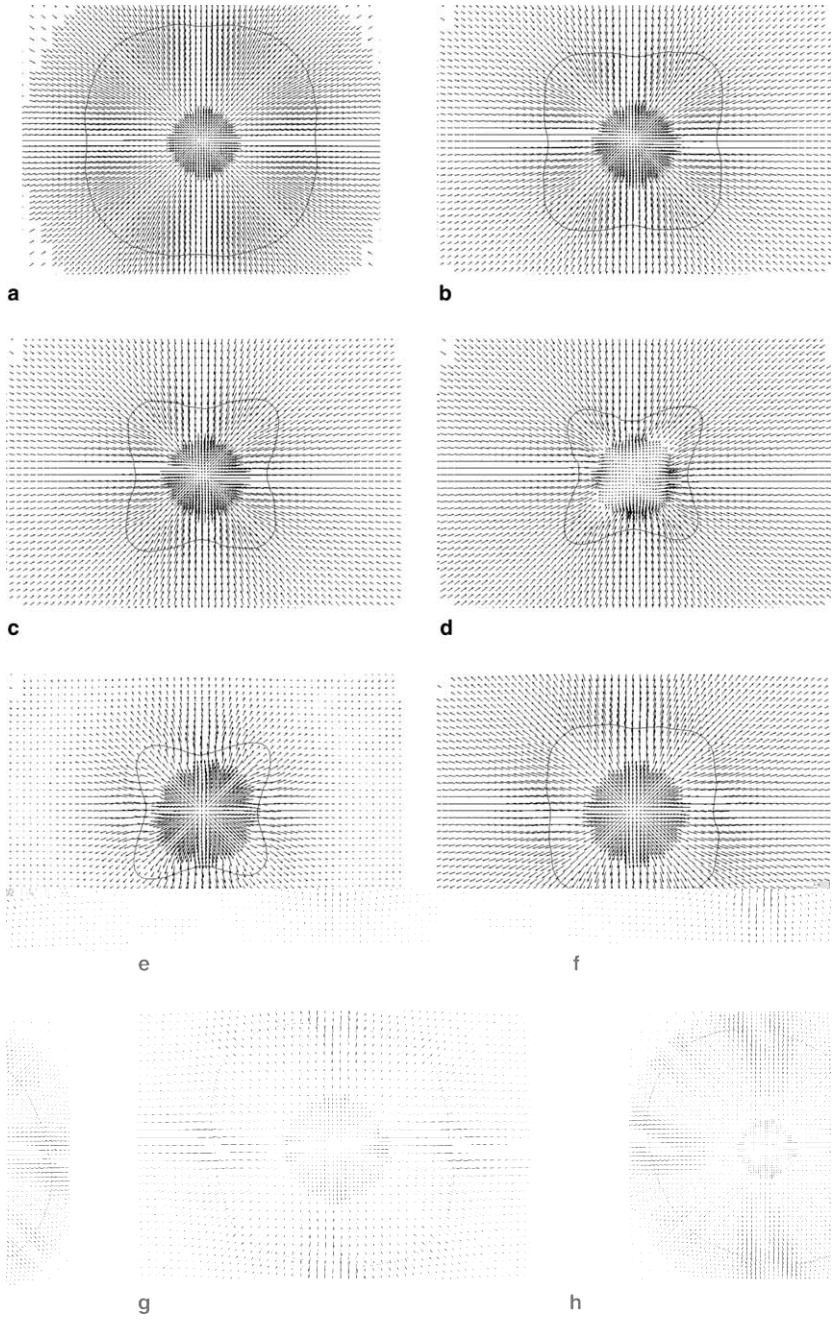

Fig. 19. Velocity distribution during the implosion displayed on a zx-plane: (a) $t = 0.090$ μs; (b) $t = 0.093$ μs; (c) $t = 0.094$ μs; (d) $t = 0.095$ μs; (e) $t = 0.096$ μs; (f) $t = 0.098$ μs; (g) $t = 0.10$ μs; (h) $t = 0.15$ μs.

The temperature profiles seen in Figs. 20(c), 21(c), and 22(c) show the compression experienced by the fluids. Inside the gas phase, the local temperature rises to many thousands of degrees Kelvin as the gas is strongly compressed. The converging shock first rapidly increases the velocity inside the bubble (Figs. 20(a), 21(a), and 22(a)), but near the final convergence of the shock wave, the velocity is reduced due to the resistance of the gas to further compression. The flow reverses direction outward once the shock has impacted on itself at the center of the bubble. These observations are similar in all the three directions, however, the change in effective radius of the bubble measured along the three axial directions are different. Importantly, the radius measured along

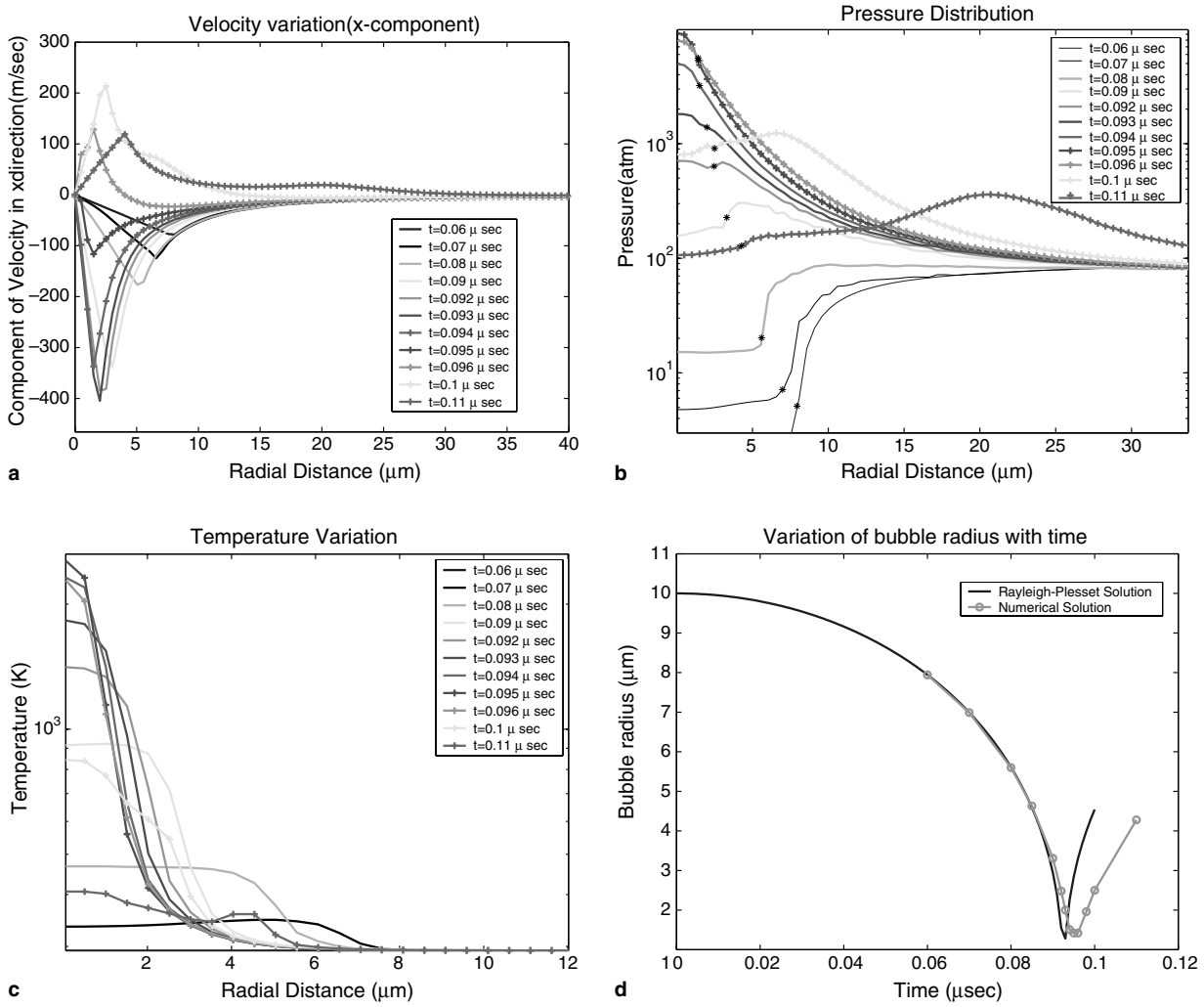

Fig. 20. Solution plotted along x-axis: (a) velocity; (b) pressure; (c) temperature; (d) radius.

the y-direction decreases even after the shock collapse, while the radii measured along x and z directions are almost stagnant during this time interval. Fig. 23 shows the analytical spherical bubble (Rayleigh–Plesset model) predictions with our DNS predictions. We can see that although the slope remains similar, there is a shift in the curve during the final stage of the implosion process and this continues through bubble rebound. This can be attributed to three-dimensional effects and shock-induced phasic compression. In addition, the Rayleigh–Plesset model does not account for any dissipative physical interactions (i.e., viscosity, heat conductivity etc.). In contrast, the mathematical model and numerical model used in DNS code accounts for viscosity, heat conductivity and compressibility of the liquid and gas. In addition, the computed 3D solution predicts an aspherical shape of the bubble rather than a radially symmetrical bubble. That is why a discrepancy between the computed solution and Rayleigh–Plesset solution happens already at the early stage of the bubble rebound. It is worth noting that the dissipation due to viscosity, heat conductivity and acoustic radiation leads to the fact that most of the kinetic energy of converging liquid is lost during bubble collapse and thus, unlike with the Rayleigh–Plesset model, the bubble does not recover the same initial radius (see Fig. 24(a)).

In addition, our DNS results clearly indicate interfacial instabilities along with the shape instabilities. The onset of interfacial instabilities can be attributed to a Taylor instability mode [52] at higher interfacial acceleration. Specifically, these classic RT instabilities occur during the later stages of implosion when the gas accelerates into the liquid. There will be a significant destabilization as the bubble nears its minimum size, since the

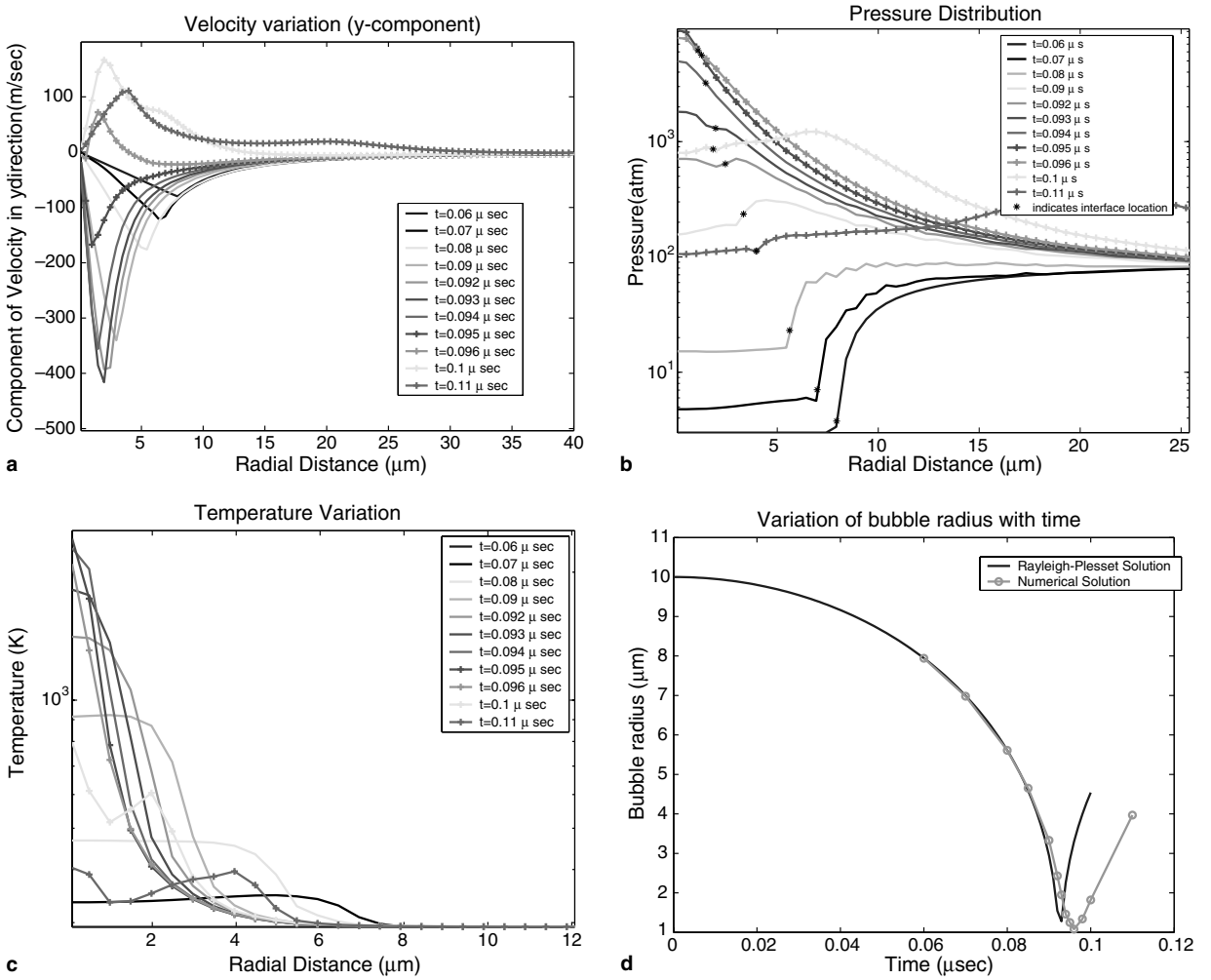

Fig. 21. Solution plotted along y-axis: (a) velocity; (b) pressure; (c) temperature; (d) radius.

acceleration of the gas towards the liquid at this time is enormous [18]. However, this effect is mitigated by the fact that the gas density also increases significantly [31].

In the present simulations, these surface instabilities were prominent only during the time interval in which the bubble radius is near its minimum and the interfacial velocities ($|\dot{R}|$) are higher than the local speed of sound of the gas. Until $t = 0.09$ μs the interface velocity is below the local speed of sound in the gas and the bubble interface remains smooth and spherical. However, once the interface velocity gets to a Mach number higher than unity, during the period of violent collapse when the interfacial accelerations were large, Figs. 17–19 show that interfacial instabilities become significant. This phenomena has been noted by many other researchers. Young [65] notes that during the final stages of bubble collapse during typical SBSL experiments, the bubble interface decelerates in preparation for re-expansion, leading to an extremely large relative acceleration of the gas with respect to the liquid, which tends to destabilize the interface. As noted previously, in our calculations it was observed that the interfacial instabilities diminish once the bubble's interface acceleration reduces (i.e., deceleration begins) and switches sign during bubble rebound. It is important to stress that the rough bubble interface see in Figs. 14 and 15 is due to physical instabilities rather than insufficient mesh resolution. Indeed care was taken to have a quality mesh with the required number of elements to adequately represent the bubble's surface even at the minimum size of the bubble. Although we have not presented the results here, the simulations were performed for different resolutions of the mesh, and it did not change the

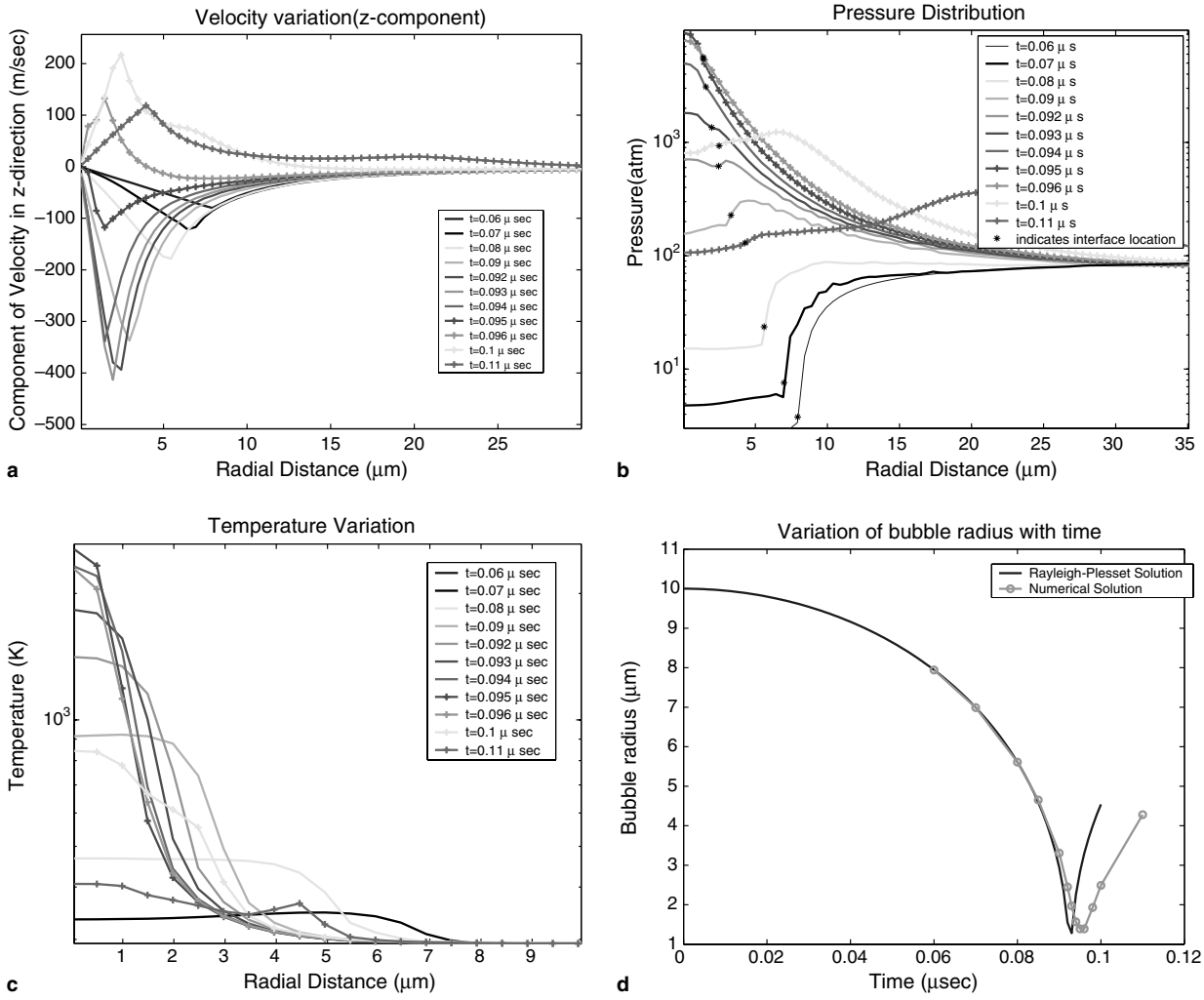

Fig. 22. Solution plotted along z-axis: (a) velocity; (b) pressure; (c) temperature; (d) radius.

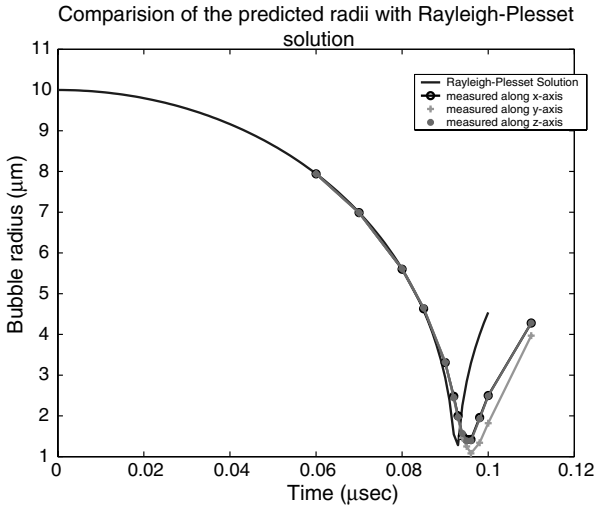

Fig. 23. Comparison of radii.

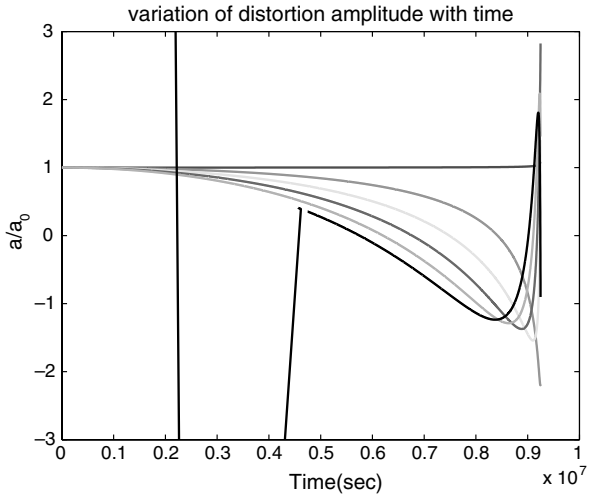

qualitative nature of the results on the interfacial and shape instabilities. Moreover, neither the time at which the minimum bubble volume was achieved, nor the characteristics of the collapse and rebound changed with the resolution of the mesh.

6. Conclusions

The current work presents a robust computational algorithm to handle compressible multiphase flows with strong shocks. The inherent abilities of this novel FEM-based computational strategy, which uses both the level set approach and ghost fluid method, was demonstrated. Using this method, a 3-D hydrodynamic shock code simulation of an imploding air bubble in a compressible liquid (water) was performed. A transient three-dimensional solution was presented for an implosion and rebound of the bubble. The results were compared with the Rayleigh–Plesset analysis and found to be in good agreement for most of the implosion process. The deviation during the final, high Mach number, stage of bubble collapse and rebound was attributed to fluid compressibility effects and the aspherical shape of the bubble. The results show that our method is capable of simulating a spherically converging shock wave. The spherical asymmetries arising from bubble implosion were captured and the existence of shape and interfacial instabilities were found.

Among the different problems which are of interest for single bubble sonoluminescence (SBSL), the stability of the bubble's shape is one of the most significant. Indeed, the resultant non-linear oscillations and the stability of the bubble are strongly influenced by the bubble shape. Researchers have independently studied this effect by perturbing the shape of the bubble numerically [45]. In this paper, we have shown that the bubble collapses with multiple harmonics rather than with a single spherical harmonic. Also, the current work clearly shows the temporal evolution of both shape and interfacial instabilities. This is significant in view of the various propositions [31] suggesting that the instabilities are responsible for the extinction of sonoluminescence [64,18,5].

The DNS simulations can advance our understanding of the bubble dynamics involved in these unstable regimes as well. We hope our results will instigate more efforts to use DNS as a tool to capture the complex dynamics involved in both single and multiple bubble implosions. Future 3-D studies should use more realistic equations of state and concentrate on the DNS simulations of externally forced oscillations of a bubble. This type of study could be done by imposing the time dependent boundary conditions at the domain boundary. These studies should show the effect of non-spherical shape on the oscillations. Furthermore, one can also perform parametric studies on the implosion of cavitation of bubble clusters to help understand the huge liquid pressure intensifications that occur within a bubble cluster [5], and to study the transient shape of the interacting bubbles within an imploding bubble cluster. Studies of this kind can help determine the key microscopic

variables that controls the various associated phenomena [59]. In the present work, we did not consider the mass transfer and have ignored phase change, However, these effects have been considered in more comprehensive studies of sonoluminescence and sonofusion [29,36]. Nevertheless, the present studies indicate that the algorithm developed for the analysis of bubble implosion should be inherently capable of representing all of the fundamental phenomena discussed herein.

Acknowledgments

The authors acknowledge the support given to this study by a USDOE-NEER grant, DOE-FG02-99ID13776, and NSF 9985340. This work was partially supported by National Computational Science Alliance under MCA01S014N and utilized both the Silicon Graphics Origin 2000 system and an IA-64 Linux cluster.

Appendix A. Coefficient matrices

The following constants have been used to write the matrices described in the appendix:

$$e_1^p = \left(\frac{\partial \rho}{\partial p}\right)_T e^{\text{tot}} + \rho\left(\frac{\partial e}{\partial p}\right)_T, \quad e_2^p = e_1^p + 1, \tag{A-1}$$

$$e_3^p = \rho e^{\text{tot}} + p, \quad e_4^p = \left(\frac{\partial \rho}{\partial T}\right)_p e^{\text{tot}} + \rho\left(\frac{\partial e}{\partial T}\right)_p. \tag{A-2}$$

After substituting the partial derivatives, the above equations simplify to:

$$e_1^p = \rho\beta_T e_1 - \alpha_p T, \quad e_2^p = e_1^p + 1, \tag{A-3}$$

$$e_3^p = \rho e_1 + p, \quad e_4^p = -\rho\alpha_p e_1 + \rho c_p. \tag{A-4}$$

The matrix $\boldsymbol{A}_0 = \boldsymbol{U}_{,\boldsymbol{Y}}$ is given by

$$\boldsymbol{A}_0 = \begin{bmatrix} \rho\beta_T & 0 & 0 & 0 & -\rho\alpha_p \\ \rho\beta_T u_1 & \rho & 0 & 0 & -\rho\alpha_p u_1 \\ \rho\beta_T u_2 & 0 & \rho & 0 & -\rho\alpha_p u_2 \\ \rho\beta_T u_3 & 0 & 0 & \rho & -\rho\alpha_p u_3 \\ e_1^p & \rho u_1 & \rho u_2 & \rho u_3 & e_4^p \end{bmatrix}. \tag{A-5}$$

The Euler–Jacobians, $\boldsymbol{A}_i = \boldsymbol{F}^{\text{adv}}{}_{i,\boldsymbol{Y}}$, are given by:

$$\boldsymbol{A}_1 = \begin{bmatrix} \rho\beta_T u_1 & \rho & 0 & 0 & -\rho\alpha_p u_1 \\ \rho\beta_T u_1^2 + 1 & 2\rho u_1 & 0 & 0 & -\rho\alpha_p u_1^2 \\ \rho\beta_T u_{12} & \rho u_2 & \rho u_1 & 0 & -\rho\alpha_p u_{12} \\ \rho\beta_T u_{31} & \rho u_3 & 0 & \rho u_1 & -\rho\alpha_p u_{31} \\ u_1 e_2^p & e_3^p + \rho u_1^2 & \rho u_{12} & \rho u_{31} & u_1 e_4^p \end{bmatrix}, \tag{A-6}$$

$$\boldsymbol{A}_2 = \begin{bmatrix} \rho\beta_T u_2 & 0 & \rho & 0 & -\rho\alpha_p u_2 \\ \rho\beta_T u_{12} & \rho u_2 & \rho u_1 & 0 & -\rho\alpha_p u_{12} \\ \rho\beta_T u_2^2 + 1 & 0 & 2\rho u_2 & 0 & -\rho\alpha_p u_2^2 \\ \rho\beta_T u_{23} & 0 & \rho u_3 & \rho u_2 & -\rho\alpha_p u_{23} \\ u_2 e_2^p & \rho u_{12} & e_3^p + \rho u_2^2 & \rho u_{23} & u_2 e_4^p \end{bmatrix}, \tag{A-7}$$

$$\boldsymbol{A}_3 = \begin{bmatrix} \rho\beta_T u_3 & 0 & 0 & \rho & -\rho\alpha_p u_3 \\ \rho\beta_T u_{31} & \rho u_3 & 0 & \rho u_1 & -\rho\alpha_p u_{31} \\ \rho\beta_T u_{23} & 0 & \rho u_3 & \rho u_2 & -\rho\alpha_p u_{23} \\ \rho\beta_T u_3^2 + 1 & 0 & 0 & 2\rho u_3 & -\rho\alpha_p u_3^2 \\ u_3 e_2^p & \rho u_{31} & \rho u_{23} & e_3^p + \rho u_3^2 & u_3 e_4^p \end{bmatrix}. \tag{A-8}$$

If we define the constant $\chi = \lambda + 2\mu$, the diffusivity coefficient matrices $\boldsymbol{K}_{ij}$ are given by:

$$\boldsymbol{K}_{11} = \begin{bmatrix} 0 & 0 & 0 & 0 & 0 \\ 0 & \chi & 0 & 0 & 0 \\ 0 & 0 & \mu & 0 & 0 \\ 0 & 0 & 0 & \mu & 0 \\ 0 & \chi u_1 & \mu u_2 & \mu u_3 & \kappa \end{bmatrix}, \tag{A-9}$$

$$\boldsymbol{K}_{12} = \begin{bmatrix} 0 & 0 & 0 & 0 & 0 \\ 0 & 0 & \lambda & 0 & 0 \\ 0 & \mu & 0 & 0 & 0 \\ 0 & 0 & 0 & 0 & 0 \\ 0 & \mu u_2 & \lambda u_1 & 0 & 0 \end{bmatrix}, \tag{A-10}$$

$$\boldsymbol{K}_{13} = \begin{bmatrix} 0 & 0 & 0 & 0 & 0 \\ 0 & 0 & 0 & \lambda & 0 \\ 0 & 0 & 0 & 0 & 0 \\ 0 & \mu & 0 & 0 & 0 \\ 0 & \mu u_3 & 0 & \lambda u_1 & 0 \end{bmatrix}, \tag{A-11}$$

$$\boldsymbol{K}_{21} = \begin{bmatrix} 0 & 0 & 0 & 0 & 0 \\ 0 & 0 & \mu & 0 & 0 \\ 0 & \lambda & 0 & 0 & 0 \\ 0 & 0 & 0 & 0 & 0 \\ 0 & \lambda u_2 & \mu u_1 & 0 & 0 \end{bmatrix}, \tag{A-12}$$

$$\boldsymbol{K}_{22} = \begin{bmatrix} 0 & 0 & 0 & 0 & 0 \\ 0 & \mu & 0 & 0 & 0 \\ 0 & 0 & \chi & 0 & 0 \\ 0 & 0 & 0 & \mu & 0 \\ 0 & \mu u_1 & \chi u_2 & \mu u_3 & \kappa \end{bmatrix}, \tag{A-13}$$

$$\boldsymbol{K}_{23} = \begin{bmatrix} 0 & 0 & 0 & 0 & 0 \\ 0 & 0 & 0 & 0 & 0 \\ 0 & 0 & 0 & \lambda & 0 \\ 0 & 0 & \mu & 0 & 0 \\ 0 & 0 & \mu u_3 & \lambda u_2 & 0 \end{bmatrix}, \tag{A-14}$$

$$\boldsymbol{K}_{31} = \begin{bmatrix} 0 & 0 & 0 & 0 & 0 \\ 0 & 0 & 0 & \mu & 0 \\ 0 & 0 & 0 & 0 & 0 \\ 0 & \lambda & 0 & 0 & 0 \\ 0 & \lambda u_3 & 0 & \mu u_1 & 0 \end{bmatrix}, \tag{A-15}$$

$$\boldsymbol{K}_{32} = \begin{bmatrix} 0 & 0 & 0 & 0 & 0 \\ 0 & 0 & 0 & 0 & 0 \\ 0 & 0 & 0 & \mu & 0 \\ 0 & 0 & \lambda & 0 & 0 \\ 0 & 0 & \lambda u_3 & \mu u_2 & 0 \end{bmatrix}, \tag{A-16}$$

$$\boldsymbol{K}_{33} = \begin{bmatrix} 0 & 0 & 0 & 0 & 0 \\ 0 & \mu & 0 & 0 & 0 \\ 0 & 0 & \mu & 0 & 0 \\ 0 & 0 & 0 & \chi & 0 \\ 0 & \mu u_1 & \mu u_2 & \chi u_3 & \kappa \end{bmatrix}. \tag{A-17}$$

The entropy variable vector is given by

$$\boldsymbol{V} = \frac{1}{T}\begin{bmatrix} \tilde{\mu} - |\boldsymbol{u}|^2/2 & u_1 & u_2 & u_3 & -1 \end{bmatrix}, \tag{A-18}$$

where $\tilde{\mu} = e + p/\rho - Ts$ is the chemical potential per unit mass, and s is the entropy.

References

[1] I. Akhatov, R. Mettin, C.D. Ohl, U. Parlitz, W. Lauterborn, On the forced oscillations of a small gas bubble in a spherical liquid-filled flask, Phys. Rev. E 55 (1997) 3747–3750.
[2] T. Barth, J.A. Sethian, Numerical schemes for the Hamilton–Jacobi and level set equations on triangulated domains, J. Comput. Phys. 145 (1998) 1–40.
[3] D. Benson, Computational methods in Lagrangian and Eulerian hydrocodes, Comp. Meth. Appl. Mech. Eng. 99 (1992) 235.
[4] J.U. Brackbill, D.B. Kothe, C. Zemach, A continuum method for modeling surface tension, J. Comput. Phys. 100 (1992) 335–354.
[5] C. Brennen, Cavitation and Bubble Dynamics, Oxford University Press, New York, 1995.
[6] M.P. Brenner, S. Hilgenfeldt, D. Lohse, R.R. Rosales, Accoustic energy storage in single bubble sonoluminescence, Phys. Rev. Lett. 77 (1996) 3467–3470.
[7] A.N. Brooks, T.J.R. Hughes, Streamline upwind/Petrov–Galerkin formulations for convection dominated flows with particular emphasis on the incompressible Navier–Stokes equations, Comp. Meth. Appl. Mech. Eng. 32 (1982) 199–259.
[8] Y.C. Chang, T.Y. Hou, B. Merriman, S. Osher, Eulerian capturing methods based on a level set formulation for incompressible fluid interfaces, J. Comput. Phys. 124 (1996) 449.
[9] J.-P. Coquel, Saurel, A Riemann problem based method for the resoltuion of compressible multimaterial flows, J. Comput. Phys. 137 (1997) 265.
[10] D. Enright, R. Fedkiw, J. Ferziger, I. Mitchelle, A hybrid particle level set method for improved interface capturing, J. Comput. Phys. 183 (2002) 83–116.
[11] R.P. Fedkiw, T. Aslam, B. Merriman, S. Osher, A non-oscillatory Eulerian approach to interfaces in multimaterial flows (the ghost fluid method), J. Comput. Phys. 152 (1999) 457–492.
[12] R.P. Fedkiw, B. Merriman, S. Osher, Numerical methods for a one-dimensional interface separating compressible and incompressible flows, Barriers and Challenges in Computational Fluid Dynamics, Cambridge University Press, Cambridge, 1999.
[13] L.P. Franca, S. Frey, Stabilized finite element methods: II. The incompressible Navier–Stokes equations, Comp. Meth. Appl. Mech. Eng. 99 (1992) 209–233.
[14] G. Hauke, A unified approach to compressible and incompressible flows and a new entropy-consistent formulation of the k–ϵ model, Ph.D. Thesis, Stanford University, 1995.
[15] G. Hauke, T.J.R. Hughes, A unified approach to compressible and incompressible flows, Comp. Meth. Appl. Mech. Eng. 113 (1994) 389–396.
[16] G. Hauke, T.J.R. Hughes, A comparative study of different sets of variables for solving compressible and incompressible flows, Comp. Meth. Appl. Mech. Eng. 153 (1998) 1–44.
[17] C. Herring, Theory of the pulsations of the gas bubble produced by an underwater explosion, OSRD, Rep. No. 236, 1941.
[18] S. Hilgenfeldt, D. Lohse, M.P. Brenner, Phase diagrams for sonoluminescing bubbles, Phys. Fluid 8 (1996) 2808–2826.
[19] T.J.R. Hughes, The Finite Element Method: Linear Static and Dynamic Finite Element Analysis, Prentice-Hall, Englewood Cliffs, NJ, 1987.
[20] T.J.R. Hughes, L.P. Franca, G.M. Hulbert, A new finite element formulation for fluid dynamics: VIII. The Galerkin/least-squares method for advective–diffusive equations, Comp. Meth. Appl. Mech. Eng. 73 (1989) 173–189.
[21] T.J.R. Hughes, L.P. Franca, M. Mallet, A new finite element formulation for computational fluid dynamics: I. Symmetric forms of the compressible Euler and Navier–Stokes equations and the second law of thermodynamics, Comp. Meth. Appl. Mech. Eng. 54 (1986) 223–234.
[22] T.J.R. Hughes, L.P. Franca, M. Mallet, A new finite element formulation for computational fluid dynamics: IV. A discontinuity-capturing operator for multidimensional advective–diffusive systems, Comp. Meth. Appl. Mech. Eng. 58 (1986) 329–336.
[23] T.J.R. Hughes, M. Mallet, A. Mizukami, A new finite element formulations for computational fluid dynamics: beyond SUPG, Comp. Meth. Appl. Mech. Eng. 32 (1982) 199–259.
[24] K. Jansen, Large-eddy simulation using unstructured grids, in: C. Liu, Z. Liu (Eds.), Advances in DNS/LES, Greyden Press, Columbus, OH, 1997.

[25] K.E. Jansen, A stabilized finite element method for computing turbulence, Comp. Meth. Appl. Mech. Eng. 174 (1999) 299–317.
[26] K.E. Jansen, S.S. Collis, C.H. Whiting, F. Shakib, A better consistency for low-order stabilized finite element methods, Comp. Meth. Appl. Mech. Eng. 174 (1999) 153–170.
[27] M. Kang, R.P. Fedkiw, X.D. Liu, A boundary condition capturing method for multiphase incompressible flow, J. Sci. Comput. 15 (2000) 323–360.
[28] R.T. Knapp, J.W. Dayly, F.G. Hammit, Cavitation, McGraw-Hill, New York, 1970.
[29] R.T. Lahey Jr., R.P. Taleyarkhan, R.I. Nigmatulin, I. Akhatov, Sonoluminescence and the search for bubble fusion, Adv. Heat Transf. 39 (in press).
[30] A. Lezzi, A. Prosperetti, Bubble dynamics in a compressible liquid part 2: second order theory, J. Fluid Mech. 185 (1987) 289.
[31] H. Lin, B.D. Storey, A.J. Szeri, Rayleigh–Taylor instability of violently collapsing bubbles, Phys. Fluid 8 (2002) 2925–2928.
[32] F. Losasso, R. Fedkiw, S. Osher, Spatially adaptive techniques for level set methods and incompressible flow, Comp. Fluid (in press).
[33] W.C. Moss, D.B. Clarke, J.W. White, D.A. Young, Hydrodynamic simulation of bubble collapse and picosecond sonoluminescence, Phys. Fluid 6 (1994) 2979–2985.
[34] S. Nagrath, K.E. Jansen, R.T. Lahey Jr., Computation of bubble dynamics with a stabilized finite element level set method, Comp. Meth. Appl. Mech. Eng. (in press).
[35] R.I. NigmatulinDynamics of Multiphase Media, vol. I–II, Hemisphere, New York, 1991.
[36] R.I. Nigmatulin, I.S. Akhatov, A.S. Topolnikov, R. Bolotnova, N.K. Vakhitova, R.T. Lahey Jr., R.P. Taleyarkhan, The theory of supercompression of vapor bubbles and nano-scale thermonuclear fusion, Phys. Fluid (in press).
[37] R.I. Nigmatulin, I.S. Akhatov, N.K. Vakhitova, R.T. Lahey Jr., On the forced oscillations of a small gas bubble in a spherical liquid-filled flask, J. Fluid Mech. 414 (2000) 47–73.
[38] R.I. Nigmatulin, N. Khabeev, F.B. Nagiev, Dynamics, heat and mass transfer of vapor-gas bubbles in a liquid, Int. J. Heat Mass Transf. 24 (6) (1981) 1033–1044.
[39] B.E. Noltingk, E.A. Neppiras, Cavitation produced by ultrasonics, Proc. Phys. Soc. Lond. B 63 (1950) 674.
[40] S.J. Osher, R.P. Fedkiw, Level Set Methods and Dynamic Implicit Surfaces, Springer Verlag, New York, 2002.
[41] M.S. Plesset, T.P. Mitchelle, On the stability of the spherical shape of a vapor cavity in a liquid, Q. Appl. Math. 13 (1956) 419–430.
[42] M.S. Plesset, A. Prosperetti, Bubble dynamics and cavitation, Ann. Rev. Fluid Mech. 9 (1977) 145–185.
[43] A. Prosperetti, A. Lezzi, Bubble dynamics in a compressible liquid part 1: first order theory, J. Fluid Mech. 168 (1986) 457.
[44] L. Rayleigh, The pressure developed in a liquid on the collapse of a spherical cavity, Phil. Mag. 34 (1917) 94–98.
[45] H. Sakagami, K. Nishihara, Rayleigh–Taylor instability on pusher fuel contact surface of stagnating targets, Phys. Fluid B 2 (1990) 2715–2730.
[46] F. Shakib, Finite element analysis of the compressible Euler and Navier–Stokes equations, Ph.D. Thesis, Stanford University, 1989.
[47] F. Shakib, T.J.R. Hughes, Z. Johan, A new finite element formulation for computational fluid dynamics: X. The compressible Euler and Navier–Stokes equations, Comp. Meth. Appl. Mech. Eng. 89 (1991) 141–219.
[48] M. Sussman, A.S. Almgren, J.B. Bell, L.H. Howell, P. Colella, W.L. Welcome, An adaptive level set approach for incompressible two-phase flows, J. Comput. Phys. 148 (1999) 81–124.
[49] M. Sussman, E. Fatemi, An efficient, interface preserving level set re-distancing algorithm and its application to interfacial incompressible fluid flow, SIAM J. Sci. Comput. 20 (4) (1999) 1165–1191.
[50] M. Sussman, E. Fatemi, P. Smereka, S.J. Osher, An improved level set method for incompressible two-phase flows, Comp. Fluid 27 (5–6) (1998) 663–680.
[51] M. Sussman, P. Smereka, S.J. Osher, A level set approach for computing solutions to incompressible two-phase flows, J. Comput. Phys. 114 (1994) 146.
[52] G.I. Taylor, On the stability of the spherical shape of a vapor cavity in a liquid, Proc. Roy. Soc. A 201 (1950) 192.
[53] T.E. Tezduyar, M. Behr, J. Liou, New strategy for finite element computations involving moving boundaries and interfaces. The deforming-spatial-domain/space-time procedure. I. The concept and the preliminary numerical tests, Comp. Meth. Appl. Mech. Eng. 94 (1992) 339–351.
[54] T.E. Tezduyar, M. Behr, J. Liou, New strategy for finite element computations involving moving boundaries and interfaces. The deforming-spatial-domain/space-time procedure. II. Computation of free-surface flows, two-liquid flows, and flows with drifting cylinders, Comp. Meth. Appl. Mech. Eng. 94 (1992) 339–351.
[55] T.E. Tezduyar, Y.J. Park, Discontinuity capturing finite element formulations for nonlinear convection–diffusion–reaction equations, Comp. Meth. Appl. Mech. Eng. 59 (1986) 307–325.
[56] A.K. Tornberg, Interface tracking methods with application to multiphase flows, Ph.D. Thesis, NADA, KTH, Stockholm, Sweeden, 2000.
[57] A.K. Tornberg, B. Engquist, A finite element based level set method for mutltiphase flow applications, Comput. Visual. Sci. 3 (2000) 13–101.
[58] S.O. Unverdi, G. Tryggvason, A front tracking method for viscous, incompressible, multifluid flows, J. Comput. Phys. 100 (1992) 25.
[59] G.E. Vazquez, S.J. Putterman, Temperature and pressure dependence of sonoluminescence, Phys. Rev. Lett. 85 (2000) 3037–3040.
[60] A. Wardlaw, Underwater explosion test cases, IHTR 2069 (1998).
[61] K. Weninger, S.J. Putterman, B.P. Barber, Angular correlations in sonoluminescence: diagnostic for the sphericity of a collapsing bubble, Phys. Rev. E 54 (1996) R2205–R2208.
[62] C.H. Whiting, K.E. Jansen, S. Dey, Hierarchical basis in stabilized finite element methods for compressible flows, Comp. Meth. Appl. Mech. Eng. 192 (2003) 5167–5185.
[63] C.C. Wu, P.H. Roberts, Shock wave propagation in a sonoluminescing gas bubble, Phys. Rev. Lett. 70 (1993) 3424.

[64] C.C. Wu, P.H. Roberts, Bubble shape instability and sonoluminescence, Phys. Lett. A 250 (1998) 131–136.
[65] F.R. Young, Sonoluminescence, CRC Press, Boca Raton, FL, 2004.
[66] P.W. Yu, S.L. Ceccio, G. Tryggvason, The collapse of a cavitation bubble in shear flows – a numerical study, Phys. Fluid 7 (11) (1995) 2608–2616.
[67] L. Yuan, C.Y. Ho, M.-C. Chu, P.T. Leung, Role of gas density in the stability of single-bubble sonoluminescence, Phys. Rev. E 64 (2001) 016317.